Experimental and Numerical Study of an Indoor Displacement Ventilation System

by

Seyediman Fatemiardestani

A Thesis submitted to the Faculty of Graduate Studies of

The University of Manitoba

in partial fulfilment of the requirements of the degree of

MASTER OF SCIENCE

Department of Mechanical and Manufacturing Engineering

University of Manitoba

Winnipeg

Abstract

This thesis reports a new set of experimental data and presents an in-depth analysis of the flow physics of a jet stream produced by a large quarter-round corner-mounted displacement diffuser. The air velocity, temperature and turbulence intensity inside the displacement ventilation (DV) jet have been thoroughly analyzed and compared with the reported findings of previous studies and model predictions. Furthermore, thermal comfort has been analyzed using the measured data following the ASHRAE standard.

This thesis also aims at establishing an accurate numerical approach for simulating the heat and fluid flow in a room ventilated by a DV system. The supply boundary condition has been thoroughly investigated, which includes tests of the conventional box and momentum modeling methods, and proposal of a more accurate modeling approach. In addition, the predictive accuracy of the standard k-ϵ, RNG k-ϵ, SST k-ω and RSM turbulence models has been examined against the experimental data.

Acknowledgements

I would like to express my great appreciation to my advisor, Professor Bing-Chen Wang, for his support and insightful guidance in my research, and also for his generous help in the non-academic area which greatly encouraged me during my study in Canada. My sincere thanks also go to Professor M. F. Tachie and Professor S. J. Ormiston for their advice and help on my course studies. I would also like to thank M. Koupriyanov and B. Tully from Price Industries Ltd. for their support and help.

I would also like to thank Abul Khair, Zhang Ye, QianQiu Xun, Mohammad Saeedi, Afzal Hossain and Shahin Nasseri for all the academic discussions and happy time working with them. I am grateful to all the friends I have made in Canada who have brought me joy and encouragement.

Finally, I would like to express my deep love and appreciation to my parents and brothers for their consistent and unconditional love and support.

Table of Contents

List of Figures

Nomenclature

English Symbols

A_{eff}	Effective area of the diffuser
A_{gross}	Total area of the diffuser
A_t	Total surface area of the test room
Ar	Archimedes number
b_{ij}	Anisotropic components of Reynolds stress tensor
C_1, C_2, C_3, C_4, C_5,	
C_1', C_3'	Constants in the RSM model
C_p	Specific heat of air at constant pressure
$C_{1\epsilon}$, $C_{2\epsilon}$, $C_{2\epsilon}^*$, $C_{3\epsilon}$	Constants in turbulence models
$CD_{k\omega}$	Cross-diffusion term
$CD_{k\omega}^+$	Positive portion of cross-diffusion term
D_{ij}	Turbulent diffusion term
F_1, F_2	Blending functions
g	Gravity constant
g_i	Gravity constant vector component
G_{ij}	Buoyancy production term
Gr	Grashof number
h	Enthalpy
h°	Total Enthalpy
k	Turbulence kinetic energy
$\vec{M}$	Momentum of the supply air
$\dot{m}_{nom}$	Nominal supply mass flow rate

n	Exponent in the jet velocity model
P	Pressure
P_k	Production of turbulent kinetic energy due to shear forces
P_{kb}	Production of turbulent kinetic energy due to buoyancy
Pr_t	Turbulent Prandtl number
Q	Supply flow rate
Re	Reynolds number
S	Norm of S_{ij}: $(2S_{ij}S_{ij})^{1/2}$
$\vec{S}$	Loss of momentum
S_E	Source term of the energy equation
S_{ij}	Strain rate tensor
t	Time
T	Air temperature
T_{mean}	Room mean air temperature
T_s	Supply air temperature
T_{out}	Outlet air temperature
Tu	Air turbulence intensity
U	Mean air velocity
$U_{i,j,k}$	Mean air velocity components
$u_{i,j,k}$	Air velocity fluctuation components
U_m	Maximum mean air velocity
V_{eff}	Effective supply velocity
V_{cor}	Corrected supply velocity
V_{me}	Measured supply velocity
V_{nom}	Nominal supply velocity
V_s	Supply velocity
vol	Volume of the sub-domain in which the momentum source is applied
x	Distance from the diffuser
x_0	Virtual origin of the jet

$x_{i,j,k}$	Coordinates of a Cartesian frame
y	Vertical distance from the floor

Greek Symbols

α_0, α_1, α^*, α_i	Constants in turbulence models
α_{cor}	Supply velocity correction factor
α_ϵ	Inverse effective Prandtl numbers for ϵ
α_m, β_m, λ_m, ϕ_m	Constants in the jet velocity model
β	Thermal expansion coefficient
β_0, β', β_i	Constant in turbulence models
Γ_t	Turbulent eddy thermal diffusivity
δ	Length scale of the jet
δ_{ij}	Kronecker delta function
ϵ	Dissipation rate
ϵ_{ij}	Dissipation rate tensor
η	Non-dimensionalized length scale of the jet: $\eta = y/\delta$
κ	Constant in the jet velocity model
λ	Thermal conductivity
μ_t	Turbulent viscosity of the fluid
μ_{eff}	Effective dynamic viscosity of the fluid
μ_{mol}	Molecular dynamic viscosity of the fluid
ν	kinematic viscosity of the fluid
$\hat{\nu}$	$\hat{\nu} = \mu_{eff}/\nu$
ρ	Air density
σ_ϵ, σ_k, σ_p, σ_ω	Constants in turbulence models
σ_{k1}, σ_{k2}, $\sigma_{\omega 1}$, $\sigma_{\omega 2}$	Constants in turbulence models
τ_{ij}	Molecular shear stress tensor

ϕ_{ij}	Pressure-strain term
Φ_1, Φ_2, Φ_3	Auxiliary relations functions
ω	Turbulent eddy frequency
Ω_{ij}	Rotation rate tensor

Abbreviations

3D	3-Dimensional
ASHRAE	American Society of Heating Refrigerating and Air-conditioning Engineers
CFD	Computational Fluid Dynamics
DNS	Direct Numerical Simulation
DV	Displacement Ventilation
DR	Draft Ratio
LDV	Laser Doppler Velocimetry
LES	Large-Eddy Simulation
MMLA	Micro-Macro Level Approach
PIV	Particle Image Velocimetry
RANS	Reynolds-Averaged Navier-Stokes
RMS	Root-Mean-Square
RNG	Re-Normalization Group
RSM	Reynolds Stress Model
RTD	Resistance Temperature Detectors
SIMPLE	Semi-Implicit Method for Pressure Linked Equations
SST	Shear Stress Transport
VATD	Vertical Air Temperature Difference

Chapter 1

Introduction

1.1 Background and Motivation

Since its first application in Scandinavia in 1978, use of displacement ventilation (DV) has become popular for air conditioning in modern public buildings such as airports, libraries, theaters and stadiums. In DV systems, air is typically introduced into an indoor environment through a floor-level supply diffuser with a relatively low velocity and at a temperature that is slightly lower than the effective temperature of the room. Owing to buoyant forces, the cold air undergoes a free fall close to the diffuser and spreads across the floor in a gravity current. The heat sources in the room warm the surrounding air, and this warmer air create upward convection in the from of thermal plumes which remove heat and contaminants form the occupied zone of the room. DV systems have the following advantages over the traditional mixing ventilation systems:

- DV systems are energy efficient because of the use of the higher supply air temperature and lower supply air velocity. It is possible to remove exhaust air from the room where the temperature is several degrees higher than the temperature in the occupied zone which significantly reduces the cooling load.

- In a well-designed displacement ventilation system, only the occupied zone of a room is cooled. In comparison with the traditional mixing ventilation systems

which require the entire indoor environment be conditioned, this unique feature of DV systems allows for a significant reduction in building energy consumption.

- A DV system is advantageous for improving the indoor air quality. An occupant's body acts like a heat source and generates thermal plumes which effectively displace the contaminants from the breathing zone of an occupant by buoyant forces.

Despite many advantages of DV systems, they may have some thermal comfort related issues. A frequent problem associated with DV systems is the so-called draft discomfort related to unwanted local cooling of the human body caused by cold air movement. Because air is directly supplied into the occupied zone, relatively low temperatures and high air velocities exist at the lower-leg region, which can cause draft discomfort. Also, because cold air is supplied at lower level, a stratified temperature field occurs in the room. This results in a large temperature difference between head and ankle levels which can be another cause of thermal discomfort in rooms with DV system.

In order to achieve maximum energy efficiency, best air quality and thermal comfort, the physical mechanisms underlying turbulent heat, mass and momentum transfer in a DV system need to be thoroughly studied. This chapter briefly reviews previous experimental and numerical studies that have been conducted to assess the performance of DV systems.

1.2 Experimental Studies

Over the past two decades, extensive studies have been conducted to improve the system performance and simplify the design procedure of DV systems. According to the study of Skistad [1], Chen *et al.* [2] and Nielsen [3], the flow rate, supply air temperature difference, diffuser type and location are the key parameters in determining the flow characteristics of a DV system. In a DV system, the cold air is supplied through a low-level diffuser. Due to buoyant forces, the air falls close to

the supply diffuser and generates a jet stream along the floor. The DV jet stream strongly influences the air distribution, energy efficiency and system performance. Also, the characteristics of a DV jet stream are of great importance to thermal comfort, because an air flow of a relatively high speed and low temperature at the lower-leg region can cause draft discomfort. Nielsen *et al.* [4], Zhang *et al.* [5], Lau *et al.* [6], and Einberg *et al.* [7] have studied the flow dynamics of different types of diffusers under a variety of room and air supply conditions. However, thus far, only a limited number of experiments have focused on the flow characteristics inside a DV jet (i.e., the flow region downstream of a diffuser and bounded by the floor, side walls and free-surface jet envelope). Here, the jet envelope refers to the dynamic interface between the jet stream and the low-speed (or even stagnant) background room air. Li *et al.* [8], and recently, Cehlin and Moshfegh [9] and Magnier *et al.* [10] conducted detailed measurements on the velocity and temperature fields inside DV jet streams in order to investigate the coupled momentum and thermal energy transport processes. Furthermore, previous experimental studies of DV jet streams have been conducted primarily based on jets issued from a small wall-mounted displacement diffuser, and measurement data based on DV systems of different types and sizes are still very limited in current literature. Also, the far downstream region of the DV jet stream has not been thoroughly studied in the previous experiments. In contrast to the previous studies, this research aims at reporting and analyzing a new set of experimental data on the jet stream in a large room supplied by a relatively large corner-mounted quarter-round displacement diffuser.

A DV jet is a prototypical example of a thermal wall jet, in which, the flows are often weakly turbulent and the transport of the momentum and thermal energy are tightly coupled. Previous efforts (e.g., Rajaratnam [11]) on this subject have concentrated on investigation of flow development in isothermal wall jets and empirical models for describing neutrally-buoyant jet velocity profiles. Studies on thermal wall jets are still relatively rare in literature and highly referenced velocity models for DV jets proposed by Nielsen [3] and Nordic Innovation Center [12] have only focused on the prediction of the maximum velocity decay of the jets.

The development of a DV jet is indeed complicated in flow physics. In a thermal jet, when buoyant forces are significantly smaller than inertial forces, the jet behaves like an isothermal one. On the other hand, when the buoyant forces are much greater than inertial forces, the jet develops like a thermal plume and the airflow is dominated by natural convection. In a DV jet, the ratio of buoyant forces to inertial forces is neither overly small nor overly large, and the flow, therefore, features mixing of forced and natural convection. Furthermore, as a DV jet develops in space, the velocity and temperature fields vary considerably along the jet. This means the ratio of the buoyant forces to inertial forces varies significantly along the jet stream, which further complicates the jet dynamics.

In present study, advanced measurement techniques such as low-temperature thermal anemometry and infrared whole-field thermography have been used to gather detailed information of velocity, temperature and turbulence intensity fields of the DV jet stream. An in-depth analysis of the experimental results and flow physics of the DV jet is presented. The obtained results are compared with the reported findings of previous studies and existing empirical models for the wall jet flow distribution. Furthermore, the influence of the relative strength between buoyant and inertial forces on the DV jet development is thoroughly analyzed based on the experimental data. The measured data shows that the velocity, temperature and turbulence intensity fields vary significantly along the jet stream, which in turn allows for a new refined division of the jet stream into four distinct zones.

1.3 Numerical Studies

Computational fluid dynamics (CFD) technique has become a valuable tool for predicting airflows in enclosed environments. Numerical simulation of indoor airflows can provide very detailed information of the performance of ventilation systems at a much lower cost in comparison with experimental tests. However, there are many factors influencing the predictive performance of numerical simulation for indoor

environment applications. Correct specification of the supply boundary conditions and selection of the turbulence models are among the most critical factors determining the predictive accuracy of a numerical simulation.

Most commonly used diffusers in displacement ventilation often have very complicated geometries. According to Srebric and Chen [13], a major obstacle for numerical simulation of an indoor environment lies in the fact that a diffuser typically has a relatively small size when compared with the indoor space but usually has strong momentum that needs to be either modeled or resolved. The computational expenses for fully resolving an indoor airflow from the diffuser is often prohibitively high. How to use fewer grid cells to accurately simulate diffusers is a bottleneck for CFD applications to indoor airflows.

Direct numerical simulation (DNS) for indoor airflows demands excessive computational effort and it is not adequate for numerical simulation of enclosed environments. The application of large-eddy simulation (LES) to indoor airflow simulation is limited to very simple geometries because LES also requires extremely fine grids for temporal simulation of the airflow. Thus far, the Reynolds-averaged Navier-Stokes (RANS) approach has been the most popular in CFD applications to indoor airflows owing to its relatively low computational cost, robustness and reasonable predictive accuracy.

Numerical simulation of air distribution in an indoor space ventilated by displacement ventilation is challenging, because of the complex physical nature of turbulence, transition between laminar and turbulent flow patterns, flow instability, and involvement of both forced and natural convection. In spite of previous efforts, a reliable numerical approach is still lacking for accurate prediction of displacement ventilation airflows. There are several important subjects in CFD applications to indoor flows, which include modeling of the diffusers (i.e., modeling of the diffuser supply conditions), and turbulence models. In the next two subsections, the state-of-the-art related to these two subjects will be briefly reviewed.

1.3.1 Modeling of Diffusers

In the most ideal situation, the boundary geometry and conditions of a diffuser used in a numerical simulation should be identical to the original diffuser in the physical experiments. This results in the so-called "direct description" method, which requires the actual detailed geometry of a complex diffuser be directly used in a simulation without any modeling. Studies of Skovgard and Nielsen [14] and Fontaine *et al.* [15] have included the airflow inside the diffuser in their numerical simulations. They also compared the direct description method with other simplified boundary-condition models, and further concluded that the performance of the direct description method is not necessary better. Although it is mathematically desirable to use precisely the original boundary geometry of the diffuser in a numerical simulation, the direct description method is very demanding in term of the computational cost. Furthermore, because of the sharp contrast between the very fine mesh used for precise description of the flow region near the complex diffuser surfaces and the coarse mesh used in the indoor space away from the diffuser, direct description method may impose difficulties in achieving numerical convergence.

In order to reduce the computational expenses associated with the direct description method, some innovative approaches have been reported in the literature. For example, some scholars split the room and diffuser into two domains such that the flow inside the diffuser can be simulated separately. Then, the obtained data on airflow leaving the diffuser can be used as the inlet boundary condition for setting up the numerical simulation of the indoor space. Sun and Smith [16] performed a two dimensional (2D) simulation of a complex diffuser to calculate the flow angle and magnitude, and then extended the obtained data set for three dimensional (3D) modeling of the geometry of the diffuser. Cehlin and Moshfegh [9] proposed the so-called "micro-macro level" approach (MMLA) to study the flow and thermal behavior of the air in the near-zone of a complex displacement diffuser. In their MMLA approach, the micro-level simulation of the flow inside the diffuser is simulated with a very fine mesh, which yields the data of the airflow leaving the diffuser. Then, these

input data can be coupled to the room model, i.e. the macro-level model, by using an equivalent but much simplified opening for describing the diffuser supply.

Given the fact that the description of complex supply diffusers requires a very fine mesh resolution and a high computation demand, in many numerical applications, it is necessary to use a simplified model that allows for capturing essential flow features of the diffuser. The most frequently used methods for modeling a complex supply diffuser can be categorized into the basic, box, momentum, and prescribed velocity models.

In the basic model, all the small diffuser openings (jets) are gathered into one or several simple slots, which have the same effective area as the diffuser. The effective area is the net area of a diffuser for the air stream passing through the diffuser surface. Studies of Heikkinen [17] and Emvin and Davidsson [18] modeled the supply diffuser using the basic model. In the basic model, using more slots to model a diffuser results in a more accurate prediction of air distribution. However, it is difficult to estimate the effective area of a diffuser, and Chen and Moser [19] further found that this method is not suitable for non-isothermal airflows.

Recently, Zhang *et al.* [5] developed a method to prescribe supply diffusers using many small openings which directly specifies the correct jet momentum from the diffusers while adjusts the airflow rate by changing the effective areas. This is done by assigning some CFD cells for a diffuser with a certain momentum, while other cells are randomly blocked. Their method successfully predicted the distribution of air velocity, temperature, and airborne contaminant concentration which showed a good agreement with the corresponding experimental data; however, the comparative study conducted in their research was limited to the area quite far from the diffuser.

The box model proposed by Nielsen [20] represents the diffuser boundary using an imaginary box surface surrounding the diffuser. Because the exact boundary conditions on the imaginary surfaces of the box need to be determined, experimental measurements of the flow and thermal conditions need to be conducted over the box surfaces. Xu and Niu [21] found that the box method is not suitable for simulating

flows at low Reynolds numbers, which are usually the cases in displacement ventilation (because the jet flow decays rapidly). In addition, the criteria for determining the box size seem to be in theoretical contradiction: on one hand, it requires that the box size be large enough to make the box boundaries lie within the fully developed regions of the jet; however, on the other hand, it requires that the box be as small as possible to minimize any impact of room conditions on the jets (Srebric and Chen [22]).

In the prescribed velocity model, the boundary conditions are specified with the basic model at the supply opening, while measured data at a certain distance downstream of the diffuser are imposed onto boundary conditions to correct and update the predicted values surrounding the diffuser at each time step. Luo and Roux [23] and Luo *et al.* [24] successfully used this method to add extra momentum to the diffuser inlet flow in their numerical simulation of the nozzle array on a complex diffuser surface.

If a diffuser is approximated as one opening with a correct mass flow rate, the momentum induction by the jet will be much smaller than that in reality. In view of this, Chen and Moser [19] proposed the so-called momentum method, which is intended to remedy the problem by specifying different velocities for the continuity and momentum equations in numerical modeling of a diffuser boundary. Srebric and Chen [13] compared the box method and the momentum method in their study of eight prototypical diffusers, and concluded that the momentum method should be used whenever possible because of its simplicity. Einberg *et al.* [7] further successfully used momentum method by applying it to simulation of a complex industrial air diffuser composed by a combination of a circular displacement diffuser on the top and a multi-cone diffuser at the bottom. However, according to Emvin and Davidsson [18], the momentum method works only on coarse meshes and gives qualitatively correct results. Xu and Niu [21] also found that the principle of momentum conservation of the flow field is not necessarily warranted in the momentum method.

1.3.2 Turbulence Modeling

Turbulence modeling directly affects the simulation accuracy and efficiency. The predictive performance of different turbulence models for enclosed environment has been evaluated by many studies, represented by Nielsen [25], Chen [26] and [27] and Kuznik *et al.* [28]. Zhai *et al.* [29] reviewed the most popular turbulence models that have been used for modeling air distribution in enclosed environments. Zhang *et al.* [30] evaluated the most frequently used turbulence models by comparing their prediction performance against a series of benchmark experimental results and recommended appropriate turbulence models for indoor environment simulations.

The standard k-ϵ model of Launder and Spalding [31] has been extensively used for the prediction of airflow in ventilated rooms because of its robustness, vast validations and reasonable accuracy. Davidson [32] numerically simulated the displacement ventilation flow using the standard k-ϵ model. Chen [26] evaluated the predictive performance of the k-ϵ model for simulation of a mix-convection airflow. Einberg *et al.* [7] also successfully applied the standard k-ϵ model to numerical simulation of the airflow in the near-zone of an industrial displacement diffuser, and concluded that this model was capable of predicting the air distribution with a reasonable accuracy. However, according to Zhai *et al.* [29] the standard k-ϵ model may have difficulty dealing with special room situations where high buoyancy effects and large temperature gradients are present.

The Re-Normalization group (RNG) k-ϵ model (Yakhot and Orszag [33]) has also been widely used for predicting indoor airflows with many successes. In comparison with the standard k-ϵ model, the RNG k-ϵ model takes into account the effect of smaller scales of motions and low-Reynolds number effects. Yuan *et al.* [34] and [35] simulated the airflow, temperature, and gas concentration distribution in a room with displacement ventilation using the RNG k-ϵ model and obtained good agreement with the experimental data. Zhang *et al.* [36] validated the RNG k-ϵ model in the special context of the airflow in a quarter of a classroom with displacement ventilation. The study found that the computed air temperature and velocity agreed reasonably well

with the measured data.

Stamou and Katsiris [37] used the SST k-ω, standard k-ϵ and RNG k-ϵ models to predict the air velocity and temperature distributions in a modeled office room with a displacement ventilation system. By comparing the numerical and experimental results, the study concluded that all three turbulence models can satisfactorily predict the main qualitative features of the flow with a slightly better performance from the SST model. Many existing studies indicate that the SST k-ω model has a better overall performance than the standard and RNG k-ϵ models for numerical simulation of indoor airflows. However, as indicated in the extensive review of Zhai *et al.* [29], a systematic evaluation of turbulence models needs to be further performed in order to reach a solid conclusion.

Chen [27] compared the predictive performances of three different Reynolds-stress models (RSM) with the standard k-ϵ model in the context of a mixed convection flow in a room. The results showed that the performance of the Reynolds-stress models is better than that of the k-ϵ model in terms of the prediction of the anisotropic turbulent stresses and recirculation pattern in the room. However, the Reynolds-stress models require additional computing effort compared to the k-ϵ model. Cehlin and Moshfegh [9] performed a numerical simulation of the airflow in a room with displacement ventilation using a RSM turbulence model, and observed that the obtained numerical results were in good agreement with the measurement data. However, the diffusion of the velocity and temperature was slightly under-predicted by the RSM model.

1.4 Objective of the Thesis

This thesis includes the following four major objectives:

- This research aims at compiling and analyzing a comprehensive measurement data set on the air velocity, temperature and turbulence intensity inside a DV jet issued from a large quarter-round corner-mounted displacement diffuser. The physics of the coupled thermal fluid fields will be thoroughly investigated. Furthermore, thermal comfort will be studied using the measured data following the ASHRAE standard.

- In order to investigate the effect of buoyant forces on the jet air velocity distribution, the measured values of the air velocity will be compared with the prediction of the conventional Verhoff [38] correlation equation for an isothermal wall jet velocity distribution. The DV jet maximum velocity decay model of Nielsen [3] will also be examined against the experimental data acquired in this study. As an improvement, this research also aims at developing a new model for predicting the velocity distribution inside the entire DV jet stream.

- The performance of the box and momentum methods for modeling the diffuser supply conditions will be evaluated using the numerical method in the context of displacement ventilation. Furthermore, a more accurate supply diffuser modeling is proposed by combining the box and momentum methods, and the obtained results will be compared with those predicted by the box and momentum methods.

- Finally, another important objective of this research is to examine the predictive accuracy of the standard k-ϵ, RNG k-ϵ, SST k-ω and RSM turbulence models for numerical simulation of air distribution in a room with displacement ventilation. The predicted values of the velocity, temperature and turbulence intensity fields by different turbulence models will be validated against the acquired experimental data.

1.5 Outline of the Thesis

The thesis is organized as follows. In chapter 2, the test case and measurement instruments will be introduced. The experimental setup and procedure will also be described, which includes, e.g. the steady-state condition, measurement locations and data collection process.

In chapter 3, the conventional Verhoff equation [38] for the isothermal jet velocity distribution will be introduced and the effect of buoyancy on the DV jet development will be investigated. Furthermore, the velocity decay model of Nielsen [3] for a DV jet will be reviewed and a new DV jet velocity model will be proposed.

In chapter 4, the numerical procedure and turbulence modeling will be introduced, including, e.g., the governing equations for RANS, selected turbulence models for closure of the momentum equation, mesh configuration, and numerical algorithm. In addition, the methods used for modeling the diffuser supply will be briefly described.

In chapter 5, the obtained results from the experiment are thoroughly analyzed and the measured values of jet velocity distribution are compared with those of the model predictions. Furthermore, the performances of the diffuser supply models and the turbulence models are examined against the experimental data.

In chapter 6, a summary of the major conclusions of this thesis and a discussion of the directions for possible future explorations will be presented.

Chapter 2

Physical Model and Experimental Procedure

2.1 Test Case

The experiment was carried out at the Price Industries research lab, in a test room with interior dimensions of 10.7 × 6.1 × 2.7 m (length by width by height, see figure 2.1). The air was supplied through a floor-level, corner-mounted, quarter-round displacement diffuser with a radius of 0.43 m and height of 1.52 m as shown in figure 2.2. The diffuser grille has a porosity of 20%, with 2.38 mm diameter circular holes, spaced by 4.76 mm (center to center). The supply airflow rate and temperature were adjusted to 208 l/s and 16.4 °C, respectively. The air temperature in the center of the room at the height 1.1 m was used as the room reference temperature following ASHRAE Standard 113 [39]. The heat balance in the test chamber was controlled with 6 adjustable ceiling-mounted radiant panels which were used to maintain a constant room reference temperature of 21 °C during the experiment. The air leaves the test room through a 0.58 m by 0.58 m opening located on the ceiling which is shown as the outlet on figure 2.1.

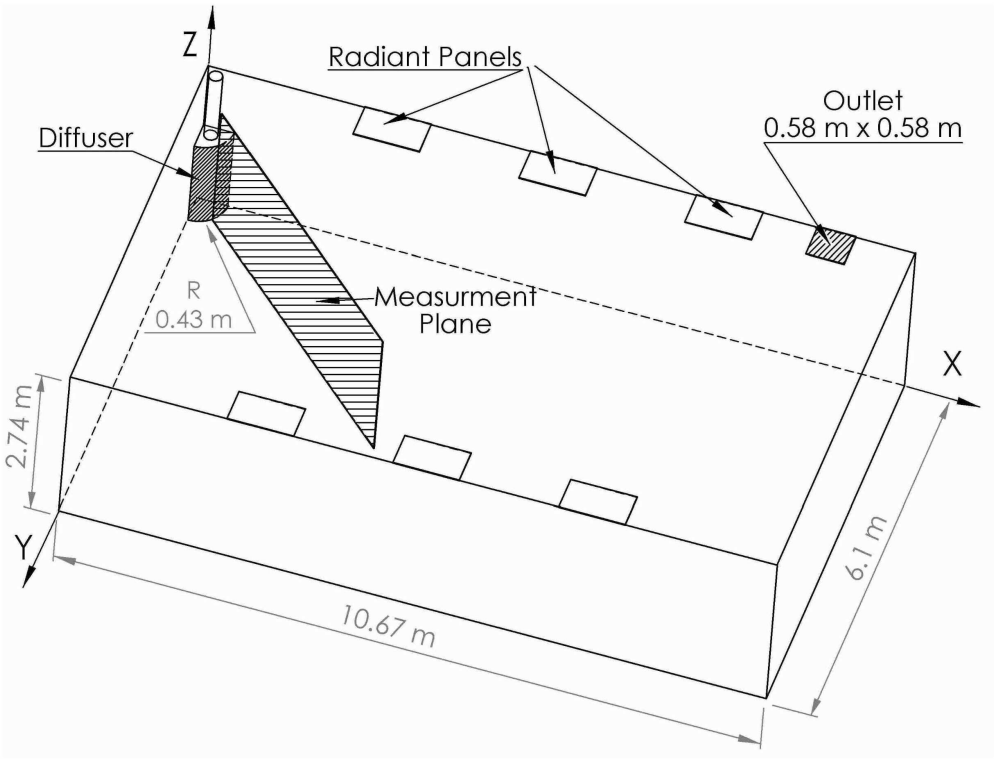

FIGURE 2.1: Schematic view of the test room, plane of measurements, radiant panels, supply diffuser and outlet.

2.2 Measurement Instruments

2.2.1 Air Velocity and Turbulence Intensity Measurement

The room airflow can be weakly turbulent, with velocities varying in magnitude, direction and fluctuating frequency. It has been indicated by Finkelstein *et al.* [40] that in the occupied zone of a room, mean air velocities range from slightly below 0.05 m/s to 0.6 m/s, turbulence intensities range from less than 10% up to 70%, and frequencies of velocity fluctuations at approximately 2 Hz contribute up to 90% of the measured standard deviation of the fluctuating velocity (or root mean squares (RMS)). In order to assess thermal comfort in a ventilated room, measurement of the mean air temperature, mean air velocity, and turbulence intensity is required according to ASHRAE standards 55 and 113.

Accurate measurement of a low air velocity is a challenging task. Available

FIGURE 2.2: The floor-level, corner-mounted, quarter-round supply displacement diffuser with a radius of 0.43 m and height of 1.52 m.

methods at present for indoor airflow measurements include thermal anemometers, ultrasonic anemometers, laser Doppler velocimetry (LDV) and particle image velocimetry (PIV). Despite the high measurement accuracy and frequency response of the LDV and PIV systems, they are less suitable for extensive measurements for full-scale room indoor airflows (Sun and Zhang [41]). Seeding the air with appropriate concentration of fine particles and covering a large measuring area when the flows are very voluminous demands enormous efforts and the costs may even be prohibitive. Commercially available ultrasonic anemometers do not offer fine spatial resolutions. The smallest ultrasonic anemometer available has a 3 cm path length between sensors which implies that the measured velocity is a mean value over the span. Hot wire thermal anemometers are suitable for measuring relatively high velocities. In a low-speed airflow field typical of an indoor environment, natural convection induced by the heat dissipated from high-temperature sensing elements becomes significant around the sensor itself, and the resulting output is consequently prone to considerable

inaccuracy (Christman and Podzimek [42]). According to Sun and Zhang [41], the measurement error is on the order of 10-25% at 0.05-0.5 m/s for a single-component hot-wire anemometer. In contrast to the above alternative methods, hot-sphere thermal anemometers were specially designed for indoor airflow applications. They are known to be reliable for measuring low air velocities in an indoor environment and are most often used in practice (Melikov *et al.* [43]). The sensors are of a spherical shape with a diameter of 1 to 3 mm and operate at a lower temperature.

Based on the above observation, the air velocity measurements were taken using two types of low-temperature thermal anemometers, TSI 8475 omni-directional hot sphere and TSI 8465 windowless anemometers (figure 2.3) in our experiment. TSI 8475 has a measurement range of 0.05-2.54 m/s with an uncertainty of $\pm 3.0\%$ in reading and $\pm 1.0\%$ in the full scale of the selected range. Due to the relatively large size of its sensing element (3 mm diameter), this type of sensor has a relatively large heat capacitance and does not offer a high temporal resolution. With a frequency response of 0.2 Hz, it was mainly used for measuring the mean velocity during the experiment. In order to measure velocity fluctuations, TSI 8465 windowless anemometers were used, which have smaller sized sensing elements and a higher frequency response of 5 Hz. The measurement range for TSI 8465 is 0.127-50.8 m/s with an uncertainty of $\pm 2.0\%$ in reading and $\pm 0.5\%$ in the full scale of the selected range. This sensor is directionally sensitive, and therefore, it needs to be carefully oriented in order to precisely measure the velocity and fluctuation magnitudes at a given position.

Thermal velocity anemometers are calibrated at a given temperature. In practice, the measured temperature of the air under study is usually different from the air temperature at which the calibration of the sensor is made. The air velocity would be measured incorrectly if the difference in these two air temperatures is not taken into account. Therefore, the transducers have an additional sensor which measures the air temperature and facilitates corrections of the measured velocity. This temperature compensation is made automatically by the thermal anemometers.

FIGURE 2.3: The low-temperature thermal anemometers: TSI 8475 omni-directional hot sphere and TSI 8465 windowless probes used for measurements of the mean air velocity and fluctuations.

According to Magnier *et al.* [10], the alignment of the anemometer affects the accuracy of the measurements. Even though the hot sphere anemometers used in this study are labeled as omni-directional, they were found to be sensitive to the airflow direction. Usually, positioning the main axis of the anemometer non-perpendicular to the airflow would lead to under-reading of the velocity magnitude. The velocity probe should be used in accordance with the manufacturer's recommendation on operation and calibration conditions. The hot sphere anemometers used in this experiment were calibrated in a small size wind tunnel with the probe positioned horizontally and perpendicular to the flow. In order to obtain more accurate results, the probes were also positioned horizontally during the experiment, identical to their position condition in the calibration.

2.2.2 Temperature Measurement

The air temperatures were measured using resistance temperature detectors (RTD) which have a measurement uncertainty of 0.1 °C (see figure 2.4). All RTD probes were calibrated at 5 temperature points before the experiment.

Measuring of the air temperature distribution in a large room is very time consuming with RTD temperature probes. It demands either many sensors or traversing of a single probe. In order to improve the measurement efficiency, infrared whole-field thermography can be considered, as it offers advantages over conventional

FIGURE 2.4: The RTD probe used in the experiment.

FIGURE 2.5: The infrared whole-field thermography camera used in the experiment.

techniques by recording real-time images of the instantaneous temperature field of a large area under investigation. In addition to RTDs, a hotshot-HD whole-field temperature infrared camera (see figure 2.5) was used to measure the air temperature near the diffuser over a measuring screen with low emissivity.

The room surface temperature measurements were performed using both thermocouples and the infrared camera. The outlet temperature was measured using a thermocouple with a standard error of 0.5 °C.

2.3 Experiment Procedure

2.3.1 Steady-State Conditions

The velocity and temperature measurements were taken under steady-state conditions. According to ASHRAE Standard 113 [39], steady-state conditions are considered to have been achieved when the volumetric quantity of the air delivered to the space does not vary by more than 10% and the difference between the temperature of the air delivered to the space and the room reference temperature does not vary by more than 1 C° during the test. The supply flow rate and temperature and room reference temperature were continuously monitored during the experiment. The supply flow rate was controlled by a variable speed fan, while the supply and reference temperature were monitored by two thermocouples. A personal computer (PC) based program was used to collect and convert the signals from the flow meter and thermocouples.

2.3.2 Measurement Locations for the Hot Sphere and RTD Probes

Smoke test were performed by Price Industries for visualization of the flow pattern in the room. As it can be seen in figure 2.6, the smoke test revealed the approximate dimensions of the jet envelope. This initial qualitative smoke test result is useful in the design of the measurement stencils and positions for the velocity and temperature probes during the follow-up experiments.

Accurate prescription of the inlet boundary conditions of a DV jet is critically important for numerical simulation of the airflow in a room (Fatemi *et al.* [44]). Therefore, in order to investigate the jet dynamics in the vicinity of the cylindrical diffuser surface and compile a data set useful for conducting and validating numerical simulations, the discharge air velocity of the diffuser was measured using a fine grid at the vicinity of the diffuser surface (2.54 cm from the diffuser surface). Because the

FIGURE 2.6: DV flow pattern visualized by smoke test.

quarter-round diffuser surface is symmetrical about central bisecting plane, detailed velocity measurements were carried out over half of the diffuser surface at angles of 5, 15, 30 and 45 degrees from the side wall.

Besides measurements of the inlet flow condition mentioned above, detailed air velocity and temperature measurements were also conducted along the streamwise direction in the so-called measurement plane (i.e., the extended central bisecting plane, 45 degree from the side wall, see figure 2.1). According to literature and our previous observation of the flow pattern in the smoke visualization test, the air velocity outside the DV jet is close to zero. Therefore, the velocity measurements were taken using a fine grid step, focusing on the vicinity of the floor and the region inside the DV jet where the largest velocity and temperature gradients are present. Figure 2.7 shows the arrangement of the velocity and temperature probes. Velocity and temperature probes are mounted together on a probe tree in the same measurement plane to expedite the data acquisition process. The RTD probes were located 4 cm downstream of the velocity probes. This was done to ensure that the sensors do not interface with each other.

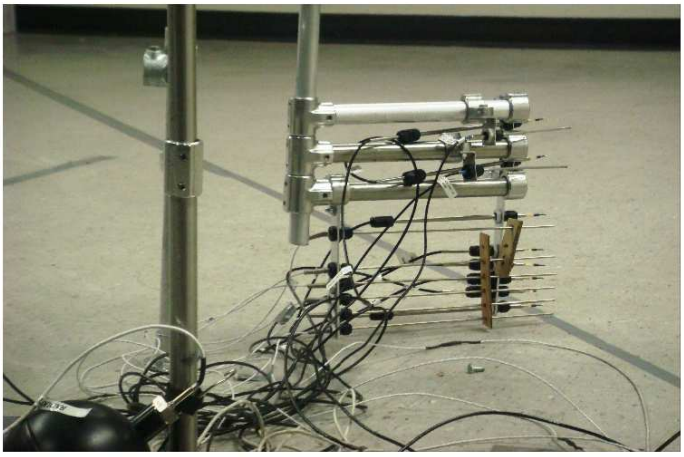

FIGURE 2.7: Arrangement of the velocity and temperature measurement probes.

2.3.3 Data Collection

At each measurement point, the air velocity and temperature were recorded for a period of three minutes following ASHRAE Standard 113 [39]. The results were used to determine the mean air velocity, mean air temperature, and turbulence intensity fields. ASHRAE Standard 113 [39] specifies a sampling rate of 0.5 Hz for measurements of the mean air velocity and temperature and a rate of 5 Hz for turbulence intensity. Measurements signals were taken at a sampling rate of 4 Hz for the mean air velocity and temperature and at a rate of 20 Hz for turbulence intensity. The output values were averaged and recorded at a rate of 2 Hz using a data acquisition system.

Chapter 3

Empirical Models

3.1 Introduction

As it is mentioned in chapter 1, the behavior of a DV jet is significantly altered by buoyant forces. In general, the DV jet dynamics depend on the ratio of buoyant forces to inertial forces. This ratio varies considerably along the jet stream. Based on experimental findings of this study, the behavior of a DV jet is very similar to that of an isothermal wall jet where the inertial forces are dominant, and the empirical velocity distribution models for an isothermal wall jet can be used approximately in the convection-dominant regions of a DV jet. On the other hand, in the regions of a DV jet where the effect of buoyancy is significant, the vertical velocity profile of the jet deviates from that of an isothermal wall jet and special velocity distribution models for DV jets need to be used for predicting the flow patterns.

In this chapter, the conventional Verhoff [38] correlation for an isothermal wall jet velocity distribution will be introduced and the effects of buoyancy on the DV jet development will be described. Furthermore, the velocity decay model of Nielsen [3] for a DV jet will be reviewed, and a new model for predicting the velocity distribution inside the entire DV jet stream will be proposed.

3.2 Wall Jet Velocity Distribution Model

The development of the velocity profile of an isothermal wall jet has been extensively studied in literature. It has been confirmed by many studies that the non-dimensional vertical velocity profiles of an isothermal wall jet at different downstream distances of the origin are self-similar. This similarity phenomenon was first reported by Forthmann [45], who non-dimensionalized velocity profiles using the maximum velocity of the jet u_m and length scale δ. The length scale δ is the jet spread defined as the vertical distance from the floor to the height where the velocity is one half of the maximum velocity. Many follow-up experimental studies such as Sigalla [46] and Myers *et al.* [47] further confirmed that velocity similarity holds generally for an isothermal wall jet. Later, Verhoff [38] proposed a dimensionless correlation to describe the self-similar mean velocity profile of an isothermal wall jet, viz.

$$u/u_m = 1.48\eta^{1/7}[1 - erf(0.68\eta)] \quad , \tag{3.1}$$

where u_m is the maximum mean jet velocity, $\eta = y/\delta$ and y is the vertical distance from the wall.

3.3 Effect of Buoyancy on Velocity Distribution

Figures 3.1 (a) and (b) show a schematic comparison of the flow development in an isothermal plane wall jet and in a DV wall jet. The jet maximum velocity and length scale are denoted by U_m and δ, respectively. As it is shown in figure 3.1 the development of a DV jet is different from that of an isothermal wall jet. A DV jet can also generate self-similar velocity profiles in the downstream region; however, its velocity field is significantly altered by buoyant forces. Owing to the existence of buoyant forces, the DV jet undergoes a free fall close to the inlet and accelerates in the vertical direction. Then the DV jet changes its direction tangent to the floor and generates a wall jet stream along the floor. The existing vertical temperature

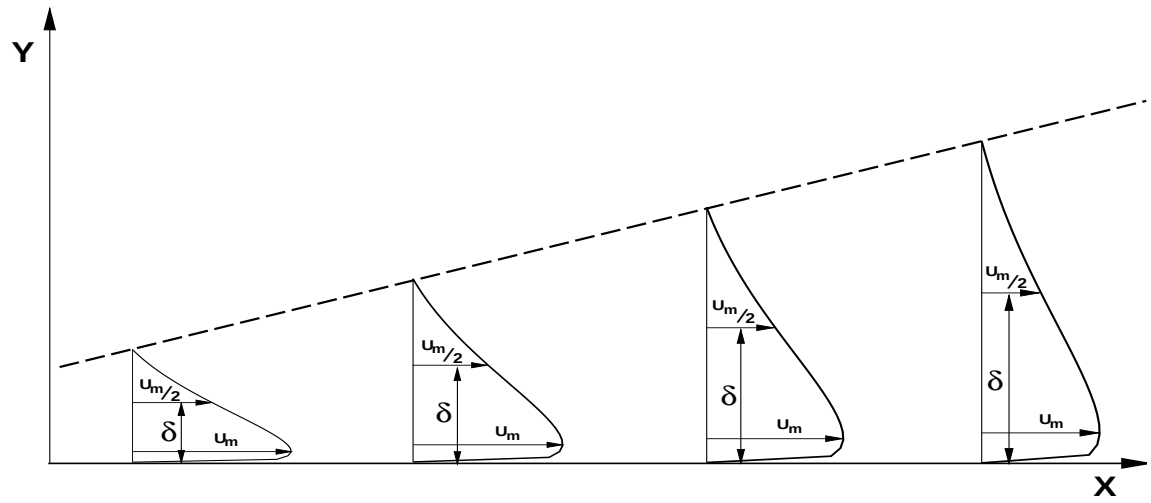

(a) Isothermal plane wall jet

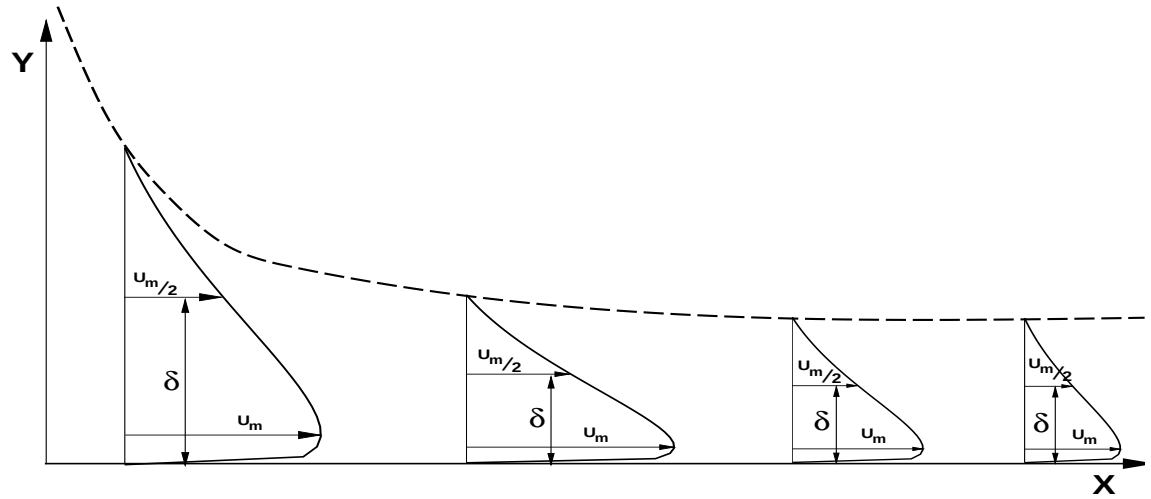

(b) DV jet

FIGURE 3.1: Schematic comparison of the flow development in an isothermal plane wall jet and a DV wall jet.

gradient works against the mixing and induction of the flow and the height of the DV jet stays rather constant downstream of the inlet. However, in an isothermal plane wall jet, the interaction of large eddies with small eddies in the interface increases the entrainment of the flow and the jet significantly spreads in the vertical direction.

According to the studies of Schwarz and Cosart [48] and Rajaratnam [11], the development of length scale δ is proportional to the distance from the jet exit in an isothermal wall jet. In contrast, it is found by Nielsen [3] that in a DV thermal wall jet, the length scale maintains rather constant as the Archimedes number increases.

The Archimedes number quantifies the ratio of the buoyant force to the inertial force and is useful for describing the non-isothermal behavior of a jet dominated by both natural and forced convection. The Archimedes number parametrizes the relative strength of natural and forced convection by evaluating the ratio of Grashof number to the square of Reynolds number:

$$Ar = Gr/Re^2 \quad . \tag{3.2}$$

The Archimedes number represents the ratio of buoyant and inertial forces, and quantifies the degree of natural convection. When $Ar >> 1$, natural convection dominates; and when $Ar << 1$, forced convection dominates. Specific to the low-speed airflow introduced by a diffuser in an indoor environment, the Archimedes number is given by:

$$Ar = \frac{g\beta h(T_{mean} - T_s)}{V_{nom}^2} \quad , \tag{3.3}$$

where β, g and h are volumetric thermal expansion coefficient, gravitational acceleration and length scale of the diffuser, respectively. $T_{mean} - T_s$ is the difference between the supply and mean room temperatures, and V_{nom} is the nominal supply velocity of the diffuser.

Later in chapter 5, the effect of buoyant forces on the behavior of a DV jet will be analyzed using the experimental data. The non-dimensionalized measured vertical velocity profiles in different zones of the DV jet will be compared with the prediction of the Verhoff model [38] for isothermal wall jets.

3.4 DV Jet Velocity Distribution Models

3.4.1 Maximum Velocity Decay Model for DV Jets

Conventional velocity distribution models for DV jets proposed by Neilsen [3] and Nordic Innovation Center [12] are known as the so-called maximum velocity decay models. According to Nielsen [4], the maximum jet velocity in the downstream region

of the DV jet can be predicted using the following equation:

$$U_m = \kappa\left(\frac{1}{x + x_0}\right)^n \quad , \tag{3.4}$$

where x_0 is the virtual origin of the jet, n is an exponent close to 1, and κ is a function of Archimedes number.

3.4.2 A New Velocity Distribution Model

In view of the restrictions of the previous maximum velocity decay models, in this research, a general velocity distribution model is proposed. The proposed model is capable of predicting the velocity at an arbitrary height (y) within a DV jet in the downstream region. Based on our experimental evidence, it is found that n and κ can actually be expressed using a linear and logarithmic functions of y, respectively:

$$n = \alpha_m y + \beta_m \quad , \tag{3.5}$$

$$\kappa = \lambda_m \ln y + \phi_m \quad . \tag{3.6}$$

Therefore, the velocity within a DV jet can be further expressed as:

$$U = (\lambda_m \ln y + \phi_m)\left(\frac{1}{x + x_0}\right)^{\alpha_m y + \beta_m} \quad . \tag{3.7}$$

In chapter 5, the predicated results using the maximum velocity decay model presented by Neilsen [3] and the model proposed here will be validated against the obtained experimental data.

Chapter 4

Numerical Procedure and Modeling

4.1 Governing Equations

For a three-dimensional non-isothermal turbulent flow, the set of governing equations includes the continuity, momentum and thermal energy equations. Based on ensemble-averaging, the system of governing equations for conducting the Reynolds-averaged Navier-Stokes (RANS) simulations take the following form:

$$\frac{\partial \rho}{\partial t} + \frac{\partial}{\partial x_j}(\rho U_j) = 0 \quad , \tag{4.1}$$

$$\frac{\partial \rho U_i}{\partial t} + \frac{\partial}{\partial x_i}(\rho U_i U_j) = -\frac{\partial p}{\partial x_i} + \frac{\partial}{\partial x_j}(\tau_{ij} - \rho\overline{u_i u_j}) + \rho[\beta(T_0 - T)]g_i \quad , \tag{4.2}$$

$$\frac{\partial \rho h^\circ}{\partial t} - \frac{\partial p}{\partial t} + \frac{\partial}{\partial x_j}(\rho U_j h^\circ) = \frac{\partial}{\partial x_j}(\lambda\frac{\partial T}{\partial x_j} - \rho\overline{u_j h}) + \frac{\partial}{\partial x_j}[U_i(\tau_{ij} - \rho\overline{u_i u_j})] + S_E \quad , \tag{4.3}$$

with the total enthalpy defined as:

$$h^\circ = h + \frac{1}{2}U_i U_j + k \quad , \tag{4.4}$$

and the turbulent kinetic energy defined as:

$$k = \frac{1}{2}\overline{u_i u_i} \quad , \tag{4.5}$$

respectively. In the above equations, the buoyant body force is computed based on the Boussinesq model and thermal radiation is neglected. The mean and fluctuating components of the velocity fields are represented using U_i and u_i, respectively. β is the thermal expansion coefficient, λ is the thermal conductivity, g_i represents the local gravitational acceleration, $\tau_{ij} = \mu(\frac{\partial U_i}{\partial x_j} + \frac{\partial U_j}{\partial x_i}) - \frac{2}{3}\mu\frac{\partial U_k}{\partial x_k}\delta_{ij}$ represents the molecular shear stress tensor, δ_{ij} is the Kronecker delta, and S_E represents heat sources in the room. To simplify the notations, over-bars are dropped from all mean flow quantities. As a result of ensemble-averaging, the Reynolds stress tensor $-\rho\overline{u_i u_j}$ and turbulent heat flux vector $-\rho\overline{u_j h}$ appear in the above set of governing equations, which need to be modeled in order to close the equation set. In the following section, the theoretical background of turbulence models used in this study is briefly described.

4.2 Turbulence Modeling

In this research, three eddy viscosity-based two equations turbulence models (Standard k-ϵ model, RNG k-ϵ Model and SST k-ω Model) and a Reynolds Stress Model (RSM) are used to close the governing equations.

4.2.1 Eddy Viscosity-based Models

For the eddy-viscosity two-equation RANS models, the Reynolds stresses are linearly related to the mean rate of strain by a scalar eddy viscosity (Boussinesq eddy viscosity assumption) as follows (Ferziger and Peric [49]; Wilcox [50]):

$$-\rho\overline{u_i u_j} = \mu_t\big(\frac{\partial U_i}{\partial x_j} + \frac{\partial U_j}{\partial x_i}\big) - \frac{2}{3}\delta_{ij}\big(\rho k + \mu_t\frac{\partial U_k}{\partial x_k}\big) \quad , \tag{4.6}$$

The turbulent heat flux is modeled as:

$$-\rho\overline{u_i h} = \Gamma_t\frac{\partial h}{\partial x_i} \quad , \tag{4.7}$$

where Γ_t is the turbulent eddy thermal diffusivity which relates to the eddy viscosity as:

$$\Gamma_t = \frac{\mu_t}{Pr_t} \quad , \tag{4.8}$$

here Pr_t is the turbulent Prandtl number.

The standard k-ϵ, RNG k-ϵ and SST k-ω turbulence models are summarized briefly below.

4.2.1.1 Standard k-ϵ Model

The standard k-ϵ model consists of the following transport equations for k and ϵ, respectively,

$$\frac{\partial(\rho k)}{\partial t} + \frac{\partial}{\partial x_i}(\rho U_i k) = \frac{\partial}{\partial x_j}\big[(\mu + \frac{\mu_t}{\sigma_k})\frac{\partial k}{\partial x_j}\big] + P_k + P_{kb} - \rho\epsilon \quad , \tag{4.9}$$

$$\frac{\partial(\rho \epsilon)}{\partial t} + \frac{\partial}{\partial x_i}(\rho U_i \epsilon) = \frac{\partial}{\partial x_j}\big[(\mu + \frac{\mu_t}{\sigma_\epsilon})\frac{\partial \epsilon}{\partial x_j}\big] + C_{1\epsilon}\frac{\epsilon}{k}(P_k + C_{3\epsilon}P_{kb}) - C_{2\epsilon}\rho\frac{\epsilon^2}{k} \quad , \tag{4.10}$$

where P_k is the turbulence kinetic energy production rate defined as:

$$P_k = \mu_t S^2 \quad , \tag{4.11}$$

here,

$$S = \sqrt{2 S_{ij} S_{ij}} \quad , \tag{4.12}$$

and, the resolved strain rate tensor defined as:

$$S_{ij} = \frac{1}{2}(\frac{\partial U_i}{\partial x_j} + \frac{\partial U_j}{\partial x_i}) \quad . \tag{4.13}$$

The turbulent (or eddy) viscosity, μ_t, is computed by combining k and ϵ as follows:

$$\mu_t = \rho C_\mu \frac{k^2}{\epsilon} \quad . \tag{4.14}$$

In equation 4.9, P_{kb} is the generation of turbulence kinetic energy due to buoyancy, calculated as:

$$P_{kb} = \beta g_i \frac{\mu_t}{Pr_t} \frac{\partial T}{\partial x_i} \quad , \tag{4.15}$$

where the default value of Pr_t is 0.85 (Fluent Manual [51]).

The model constants, which are determined from experiments for homogeneous shear flows and isotropic turbulence are as follows: $C_{1\epsilon} = 1.45$, $C_{2\epsilon} = 1.9$, $C_\mu = 0.09$, $\sigma_k = 1.0$ and $\sigma_\epsilon = 1.3$ (Launder and Spalding [31]).

4.2.1.2 RNG k-ϵ Model

The RNG model was developed using Re-Normalization Group (RNG) methods to re-normalize the Navier-Stokes equations to account for the effects of smaller scales of flow motion. In the standard k-ϵ model, the eddy viscosity is determined from a single turbulence length scale (i.e., the largest integral scale of turbulence), so the calculated turbulent diffusion is that which occurs only at the specified scale; whereas in reality, all scales of flow motion contribute to the turbulent diffusion. The RNG approach, which is a mathematical technique that can be used to derive a turbulence model similar to the standard k-ϵ model, results in a modified form of the ϵ equation which attempts to account for different scales of flow motion through changes to the production term. The modified form of the ϵ equation is given by:

$$\frac{\partial(\rho\epsilon)}{\partial t} + \frac{\partial}{\partial x_i}(\rho U_i \epsilon) = \frac{\partial}{\partial x_j}(\alpha_\epsilon \mu_{eff} \frac{\partial \epsilon}{\partial x_j}) + C_{1\epsilon}\frac{\epsilon}{k}(P_k + C_{3\epsilon}P_{kb}) - C^*_{2\epsilon}\rho\frac{\epsilon^2}{k} \quad , \tag{4.16}$$

where μ_{eff} is the effective viscosity defined by:

$$\mu_{eff} = \mu + \mu_t \quad , \tag{4.17}$$

The scale elimination procedure in the RNG theory results in a differential equation for turbulent viscosity:

$$d\Big(\frac{\rho^2 k}{\sqrt{\epsilon\mu}}\Big) = 1.72\frac{\hat{\nu}}{\sqrt{\hat{\nu}^3 - 1 + C_\nu}}d\hat{\nu} \quad , \tag{4.18}$$

where $\hat{\nu} = \mu_{eff}/\nu$ and $C_\nu = 100$.

Equation 4.18 is integrated to obtain an accurate description of how the effective turbulent transport varies with the effective Reynolds number, allowing the model to better handle low-Reynolds-number and near-wall flows.

In equation 4.16, coefficient α_ϵ represents the inverse effective of the Prandtl number for ϵ. It is computed using the following formula derived analytically through the RNG theory:

$$\left|\frac{\alpha_\epsilon - 1.3929}{\alpha_0 - 1.3929}\right|^{0.6321}\left|\frac{\alpha_\epsilon + 2.3929}{\alpha_0 + 2.3929}\right|^{0.3679} = \frac{\mu_{mol}}{\mu_{eff}} \quad , \tag{4.19}$$

where $\alpha_0 = 1$. Coefficient $C^*_{2\epsilon}$ is given by:

$$C^*_{2\epsilon} = C_{2\epsilon} + \frac{C_\mu \rho \eta^3 (1 - \eta/\eta_0)}{1 + \beta_0 \eta^3} \quad , \tag{4.20}$$

where $\eta = \frac{Sk}{\epsilon}$, $\eta_0 = 4.38$ and $\beta_0 = 0.012$.

The model constants $C_{1\epsilon}$ and $C_{2\epsilon}$ in equation 4.16 have values derived analytically based on the RNG theory. These values, used by default in FLUENT, are $C_{1\epsilon} = 1.42$ and $C_{2\epsilon} = 1.68$ (Fluent Manual [51]).

4.2.1.3 SST k-ω Model

The SST k-ω model combines the k-ϵ and k-ω models using a blending function. The SST model activates the k-ω model in the near-wall region and the k-ϵ model for the rest of the flow. By this approach, the high near-wall performance of the k-ω model is utilized without the potential errors resulting from its sensitivity to the free stream. The eddy viscosity is modeled with the SST model, given by:

$$\frac{\partial(\rho k)}{\partial t} + \frac{\partial}{\partial x_j}(\rho U_j k) = \frac{\partial}{\partial x_j}\Big[\frac{\partial k}{\partial x_j}\Big(\mu + \frac{\mu_t}{\sigma_k}\Big)\Big] + P_k + \beta'\rho k\omega + P_{kb} \quad , \tag{4.21}$$

$$\frac{\partial(\rho\omega)}{\partial t}+\frac{\partial}{\partial x_j}(\rho U_j\omega)=\frac{\partial}{\partial x_j}\big[\frac{\partial\omega}{\partial x_j}\big(\mu+\frac{\mu_t}{\sigma_\omega}\big)\big]+CD_{k\omega}+\alpha_i\frac{\rho}{\mu_t}P_k+\beta_i\rho\omega^2 \quad , \tag{4.22}$$

where σ_k and σ_ω are the turbulent Prandtl numbers for k and ω, respectively, given by:

$$\sigma_k=\frac{1}{F_1/\sigma_{k1}+(1-F_1)/\sigma_{k2}} \quad , \tag{4.23}$$

$$\sigma_\omega=\frac{1}{F_1/\sigma_{\omega1}+(1-F_1)/\sigma_{\omega2}} \quad . \tag{4.24}$$

In equation 4.21, P_k represents the turbulence kinetic energy production rate due to the mean velocity gradients, which has been described in equation 4.11. The eddy viscosity is then calculated using the following limiter-based formulation:

$$\mu_t=\frac{\rho k}{\omega}\frac{1}{\max(\frac{1}{\alpha^*},\frac{SF_2}{\alpha_1\omega})} \quad . \tag{4.25}$$

The generation of turbulence kinetic energy due to buoyancy, P_{kb}, calculated using equation 4.15. The cross-diffusion term, $CD_{k\omega}$, is defined as:

$$CD_{k\omega}=(1-F_1)2\rho\frac{1}{\sigma_{\omega2}\omega}\frac{\partial k}{\partial x_j}\frac{\partial\omega}{\partial x_j} \quad . \tag{4.26}$$

To reduce the model to a low Reynolds number k-ω model in the boundary layer while recovering a k-ϵ model in the free stream, the following blending functions are used:

$$F_1=\tanh(\Phi_1^4) \quad , \quad F_2=\tanh(\Phi_2^2) \quad , \tag{4.27}$$

and the auxiliary relations are computed as:

$$\Phi_1=\min(\Phi_2,\frac{4\rho k}{CD^+_{k\omega}\sigma_{\omega2}y^2}) \quad , \quad \Phi_2=\max(\frac{2\sqrt{k}}{\beta'\omega y},\frac{500\nu}{y^2\omega}) \quad , \tag{4.28}$$

$$CD^+_{k\omega}=\max(2\rho\frac{1}{\sigma_{\omega2}\omega}\frac{\partial k}{\partial x_j}\frac{\partial\omega}{\partial x_j},10^{-20}) \quad , \tag{4.29}$$

where y is the normal distance to the wall and $CD^+_{k\omega}$ is the positive portion of the cross-diffusion term defined in equation 4.26.

Model constants are as follows: $\alpha_1 = 0.31$, $\beta' = 0.09$, $\sigma_{k1} = 1.176$, $\sigma_{k2} = 1$, $\sigma_{\omega 1} = 2$ and $\sigma_{\omega 2} = 1.168$. The coefficients α_i, α^* and β_i are defined in Fluent Manual [51].

4.2.2 Reynolds Stress Model (RSM)

In contrast to the previous two-equation turbulence models utilized in this study, the RSM model calculates the Reynolds stresses from their relevant transport equations (rather than using explicit algebraic models based on the Boussinesq assumption). Thus, in a 3D flow simulation, six equations need to be solved to obtain the six independent Reynolds stresses, together with an equation for calculating the isotropic turbulence energy dissipation rate. This modeling strategy originated from the work of Launder *et al.* [52]. The Reynolds stress transport equations are expressed as:

$$\begin{aligned}\frac{\partial(\rho\overline{u_i u_j})}{\partial t} + \frac{\partial}{\partial x_k}(\rho U_k \overline{u_i u_j}) = &- \frac{\partial}{\partial x_k}[\rho\overline{u_i u_j u_k} + \overline{p(\delta_{kj}u_i + \delta_{ik}u_j)}] + \frac{\partial}{\partial x_k}(\mu\frac{\partial}{\partial x_k}(\overline{u_i u_j})) \\ &- \rho(\overline{u_i u_k}\frac{\partial U_j}{\partial x_k} + \overline{u_j u_k}\frac{\partial U_i}{\partial x_k}) - \rho\beta(g_i\overline{u_j T} + g_j\overline{u_i T}) \\ &+ \overline{p(\frac{\partial u_i}{\partial x_j} + \frac{\partial u_j}{\partial x_i})} - 2\mu\overline{\frac{\partial u_i}{\partial x_k}\frac{\partial u_j}{\partial x_k}} \quad , \end{aligned} \tag{4.30}$$

where the first and second terms on the left-hand side are transitional and convective terms, respectively. The terms on the right-hand side of equation 4.30 are the turbulent diffusion, molecular diffusion, stress production, production due to buoyancy, pressure-strain, and dissipation rate terms, respectively. Among these terms the turbulent diffusion D_{ij}, buoyancy production G_{ij}, pressure-strain ϕ_{ij} and dissipation rate ϵ_{ij} terms need to be modeled (i.e., the first, third, fourth and sixth terms, respectively). The turbulent diffusion term D_{ij} is modeled as:

$$D_{ij} = \frac{\partial}{\partial x_k}(\frac{\mu_t}{\sigma_k}\frac{\partial\overline{u_i u_k}}{\partial x_k}) \quad , \tag{4.31}$$

where $\sigma_k = 0.82$. The turbulent viscosity, μ_t, is computed using Equation 4.14. For modeling the pressure-strain term, ϕ_{ij}, the proposed quadratic model of Speziale *et*

al. [53] is used.

$$\begin{aligned}\phi_{ij} = & - (C_1\rho\epsilon + C_1'\frac{P}{2})b_{ij} + C_2\rho\epsilon(b_{ik}b_{kj} - \frac{1}{3}b_{mn}b_{mn}\delta_{ij}) + (C_3 - C_3'\sqrt{b_{ij}b_{ij}})\rho k S_{ij} \\ & + C_4\rho k(b_{ik}S_{jk} + b_{jk}S_{ik} - \frac{2}{3}b_{mn}S_{mn}\delta_{ij}) + C_5\rho k(b_{ik}\Omega_{jk} + b_{jk}\Omega_{ik}) \quad , \end{aligned} \tag{4.32}$$

where b_{ij} is the anisotropic components of the Reynolds stress tensor, defined as:

$$b_{ij} = -(\frac{\overline{u_i u_j} + \frac{2}{3}k\delta_{ij}}{2k}) \quad , \tag{4.33}$$

and the mean rate-of-rotation tensor, Ω_{ij}, is defined by:

$$\Omega_{ij} = \frac{1}{2}(\frac{\partial U_i}{\partial x_j} - \frac{\partial U_j}{\partial x_i}) \quad . \tag{4.34}$$

In equation 4.32, the model constants are set to: $C_1 = 3.4$, $C_1' = 1.8$, $C_2 = 4.2$, $C_3 = 0.8$, $C_3' = 1.3$, $C_4 = 1.25$ and $C_5 = 0.4$ (Fluent Manual [51]). The production due to buoyancy term, G_{ij}, can be modeled as:

$$G_{ij} = \beta\frac{\mu_t}{Pr_t}(g_i\frac{\partial T}{\partial x_j} + g_j\frac{\partial T}{\partial x_i}) \quad , \tag{4.35}$$

where Pr_t is the turbulent Prandtl number for energy, with a default value of 0.85. The turbulence energy dissipation rate, ϵ_{ij}, is obtained by solving a transport equation given previously by equation 4.10.

4.3 Mesh Configuration

In the current study, GAMBIT 2.2 was used to create the geometry domain and generate the mesh for numerical simulation. Both combined structured (hex/map) and unstructured (hex/cooper) meshes were used for discretizing of the computational domain. The grid dependence was checked using three different grid densities to ensure that gird resolution would not have a notable impact on the numerical results.

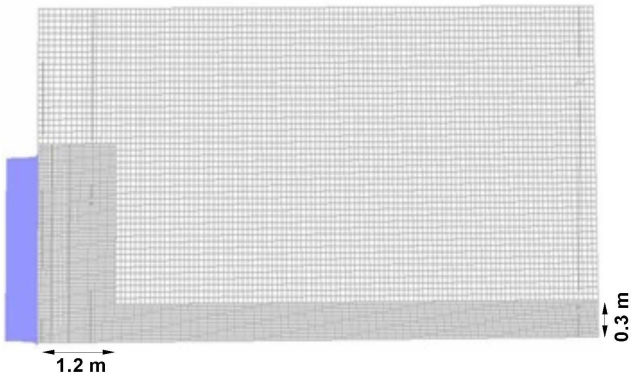

FIGURE 4.1: Mesh configuration of the computation domain (vertical view).

Specific to the test case, the mesh used in regions with larger velocity and temperature gradients should be sufficiently fine to capture the local small scale flow physics. On the other hand, in order to reduce the computational expenses, relatively coarse meshes should be applied to the rest of the domain. From the experiments, it is observed that relatively large velocity and temperature gradients are present in regions close to the floor and near the diffuser. For this reason, the grid size near the diffuser and close to the floor is set to around 0.025 m and then is increased to 0.05 m in the rest of the domain. The vertical view of the mesh configuration of the computation domain is shown in figure 4.1.

4.4 Numerical Method

The commercial solver ANSYS FLUENT version 13.0 was used for all computations. The governing equations were discretized using a finite volume technique. Pressure-velocity coupling was achieved by a SIMPLE algorithm provided by the software. The convection term in momentum, energy, turbulent kinetic energy, and dissipation rate equations were discretized using a second-order upwind scheme. The discretization of pressure equation was based on a second-order scheme. The simulated airflow was assumed to be steady and incompressible. Convergence was considered to be achieved when the sum of the total normalized residuals of the governing equations was less than 10^{-7} for thermal energy and 10^{-4} for other variables.

4.5 Boundary Conditions

4.5.1 Supply Boundary Conditions

In the present study, in order to analyze the effect of inlet boundary condition on the prediction of room airflow, the supply diffuser is modeled using box and momentum methods. Furthermore, a more accurate supply diffuser modeling approach is proposed which combines the existing box and momentum methods. This subsection briefly describes the methods used in this study for specifying the inlet boundary condition of the room airflow used in the numerical simulation.

4.5.1.1 Box Method

In the box method, the measured velocity profiles at the vicinity of the diffuser should be used as the inlet velocity boundary condition. However, the measured inlet velocity profiles indicate a higher value of the mass flow rate in comparison with the nominal mass flow rate of the diffuser. This difference has also been observed in the experimental study of Magnier *et al.* [10]. One of the reasons for this behavior lie in the mechanism of jet development. In fact, the tiny jets coming out from the small holes of the perforated diffuser surface might not merge at the vicinity of the diffuser to form an integrated jet. In the experiments, it is challenging to determine the optimum distance in front of the diffuser where the inlet velocity measurements should be conducted. From the point of view of fluid dynamics, in general, this distance has to be long enough to allow the tiny jets to merge. On the other hand, because the tiny jets decay rapidly as the distance from the diffuser increases, the distance has to be as small as possible (Xu and Niu [21]). The relatively high turbulence level and complex mixing pattern of the flow at the perforated surface of the diffuser can be the other cause of the mismatching of the mass flow rates.

In our simulation, a correction factor has been applied to the obtained velocity profile, such that the resultant inlet velocity profile after the correction produces a

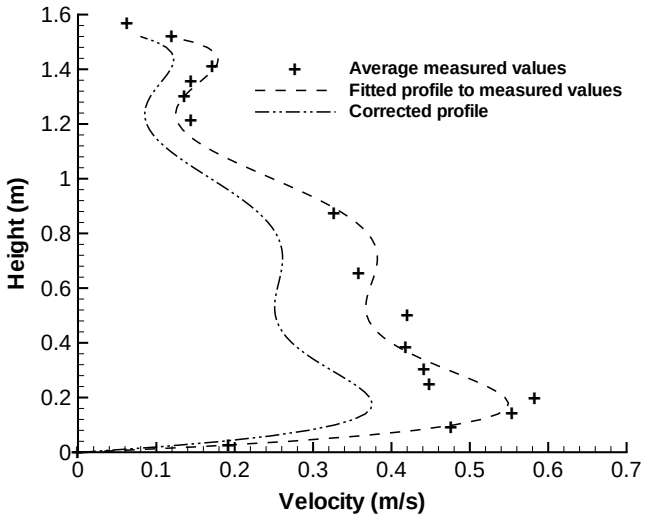

FIGURE 4.2: Corrected inlet velocity profile.

flow rate consistent with the nominal flow rate of the diffuser. The following formula is used to correct the measured inlet velocity profile:

$$V_{cor} = \alpha_{cor} V_{me} \quad , \tag{4.36}$$

where V_{cor} and V_{me} are the corrected and measured velocities, respectively. In the above equation, α_{cor} is the correction factor, defined as:

$$\alpha_{cor} = \frac{\int \rho V_{me} dA_{gross}}{\dot{m}_{nom}} \quad , \tag{4.37}$$

where A_{gross} is the total surface area of the supply diffuser, and $\dot{m}_{nom}$ is the nominal mass flow rate. The corrected inlet velocity profile and the measured velocity values in the vicinity of the diffuser (2.54 cm) are shown in figure 4.2. It shows that the proposed method represented by equation 4.36 is effective in correcting the inlet velocity profile to reproduce the nominal mass flow rate.

4.5.1.2 Momentum Method

In the momentum method, the supply diffuser in approximated as one opening of the same size of the diffuser and with a uniform velocity as follow:

$$V_s = V_{nom} = \frac{Q}{A_{gross}} \quad , \tag{4.38}$$

where V_{nom} represents the nominal supply velocity, Q is the supply flow rate and A_{gross} is the total surface area of the supply diffuser. Conservation of momentum is achieved by adding an extra momentum source term $\vec{S}$ to the momentum equation:

$$V.\nabla(\rho\vec{V}) = -\nabla p + \mu\nabla^2\vec{V} + \rho\vec{g} + \vec{S} \quad , \tag{4.39}$$

where $\vec{S}$ is the loss of momentum that needs to be added to a sub-domain behind the diffuser:

$$\vec{S} = \frac{\vec{M}}{vol} \quad , \tag{4.40}$$

with

$$\vec{M} = \rho V_{eff}^2 A_{eff} - \rho V_{nom}^2 A_{gross} \quad . \tag{4.41}$$

Here, *vol* is the volume of the sub-domain to which the momentum source is applied, $\vec{M}$ is the momentum of the flow, and A_{eff} is the effective opening area of the supply diffuser. The effective supply velocity, V_{eff}, is calculated as:

$$V_{eff} = V_{nom}\frac{A_{gross}}{A_{eff}} \quad . \tag{4.42}$$

4.5.1.3 Box-Momentum Method

Despite the challenges encounters in the measurements of the velocity close to the inlet, the velocity profiles acquired from our carefully designed experiments are of excellent quality, which allow us to combine the box and momentum methods and propose a more general approach for treating the inlet boundary condition.

For the proposed approach, similar to box method, the corrected measured velocity profile can be used for the inlet velocity boundary condition. The loss of momentum is then compensated using the following formula:

$$\vec{M} = \int \rho V_{eff}^2 dA_{eff} - \int \rho V_{cor}^2 dA_{gross} \quad , \tag{4.43}$$

where V_{eff} is calculated as:

$$V_{eff} = V_{cor} \frac{A_{gross}}{A_{eff}} \quad . \tag{4.44}$$

4.5.2 Wall Heat Flux Boundary Condition

In order to maintain the proper heat balance in the room, a uniform heat flux is applied to the walls of the room. The heat flux is calculated to maintain the measured outlet temperature of 22.3 C° with the given flow rate. The following formula is used to calculate the heat flux:

$$q = \frac{\rho Q C_p (T_{out} - T_s)}{A_t} \quad , \tag{4.45}$$

where C_p is the specific heat of the air at constant pressure, A_t is the total surface area of test room. T_s and T_{out} are the temperatures at the supply and outlet of the test room, respectively.

4.5.3 Outlet Boundary Condition

For the outlet boundary conditions, zero gradients are applied to all field variables are considered.

Chapter 5

Results and Discussions

In this chapter, the results on the experimental and numerical studies of the large quarter-round corner-mounted displacement diffuser will be presented and analyzed. Discussion of the experimental results will be first presented in subsections 5.1–5.7, and then discussion of the numerical results will be presented in subsection 5.8.

5.1 Measurements of the Inlet Velocity Boundary Condition

Figure 5.1 shows the circumferential mean air discharge velocity profiles acquired in the vicinity of the cylindrical diffuser surface at different heights during the experiment. The air velocity profiles in figure 5.1 indicate that the diffuser generates a semi-radial flow pattern in the circumferential direction between 15 and 75 degrees. The magnitude of the jet velocity reduces significantly close to side walls. As seen from the figure, this near-wall effect is the most evident at heights 0.1 m and 0.2 m above the floor, where the jet velocity reaches its maximum.

Figure 5.2 shows the vertical mean air discharge velocity profiles in the vicinity of the diffuser surface at different angles. The air velocity profiles in figure 5.2 indicate that the face velocity distribution in vertical direction varies over the diffuser surface. It reaches its maximum at about 0.2 m above the floor and then gradually decreases as the height increases.

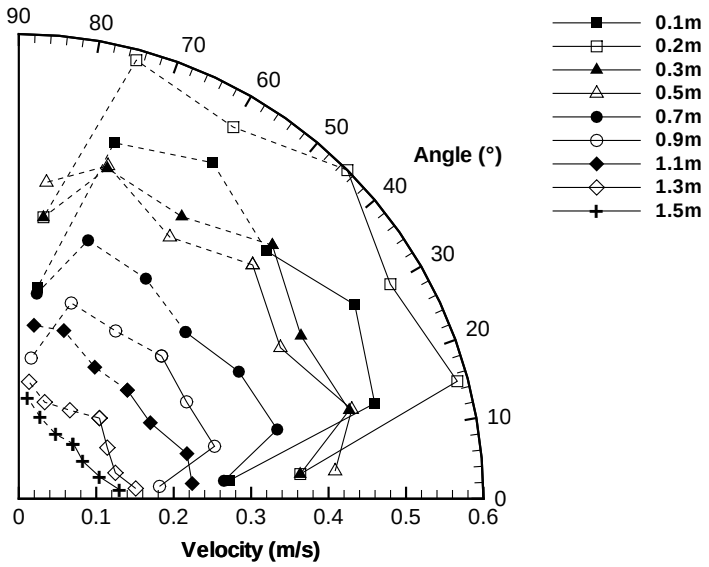

FIGURE 5.1: Circumferential velocity profiles at different heights immediately over the diffuser surface (or, at jet inlet).

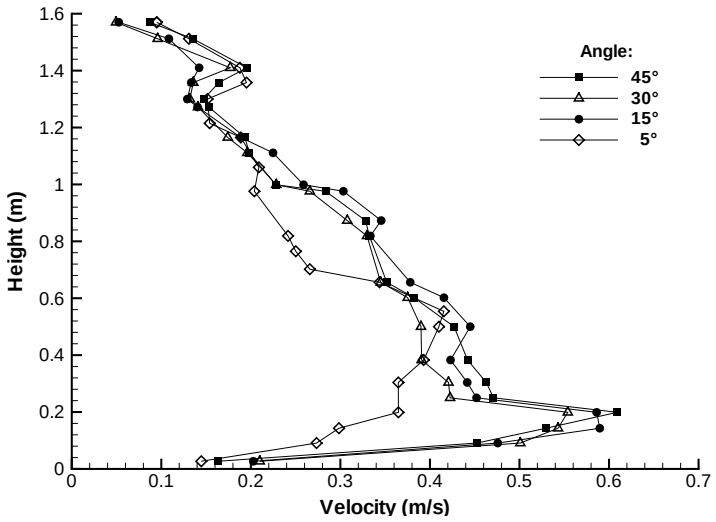

FIGURE 5.2: Vertical inlet velocity profiles at different angles over the diffuser surface (or, at jet inlet).

5.2 Experimental Results on Air Velocity Distribution

As demonstrated previously in the smoke visualization test (see figure 2.6), the airflow close to the diffuser undergoes a sudden free fall (downdraft), and the height of the

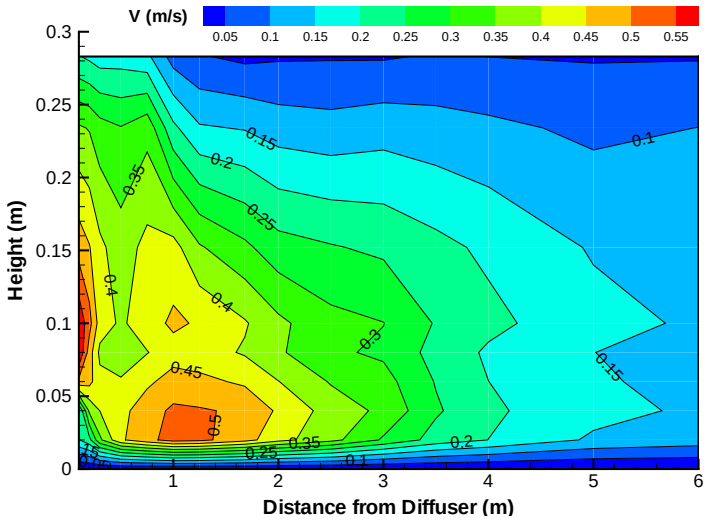

FIGURE 5.3: Contour of velocity in the measurement plane inside the DV jet.

jet envelope is much smaller than the height of the diffuser. Figure 5.3 displays the contour of velocity distribution inside the DV jet at different downstream distances from the diffuser. Due to the buoyant forces, the air accelerates in the vertical direction and reaches its maximum velocity within a short downstream distance from the diffuser. Then the jet velocity gradually decreases as the distance from the diffuser increases.

In literature, a DV jet is generally divided into two distinct zones according to its flow pattern: the primary zone, where the air velocity increases; and the secondary zone, where the air velocity decreases. The results obtained from this experiment allow us to conduct a refined analysis of the DV jet under testing. It is observed that for a floor-level DV system, the jet stream can be actually divided into four apparent zones (see figures 5.4 and 5.5): the falling zone, acceleration zone, fully developed zone and fading zone. In the following context, the physical characteristics of these four distinct zone will be discussed.

5.2.1 Falling Zone

In this zone, the cold dense jet stream leaves the diffuser and falls on the floor due to strong buoyancy forces. In the present experiment, the falling zone begins from the

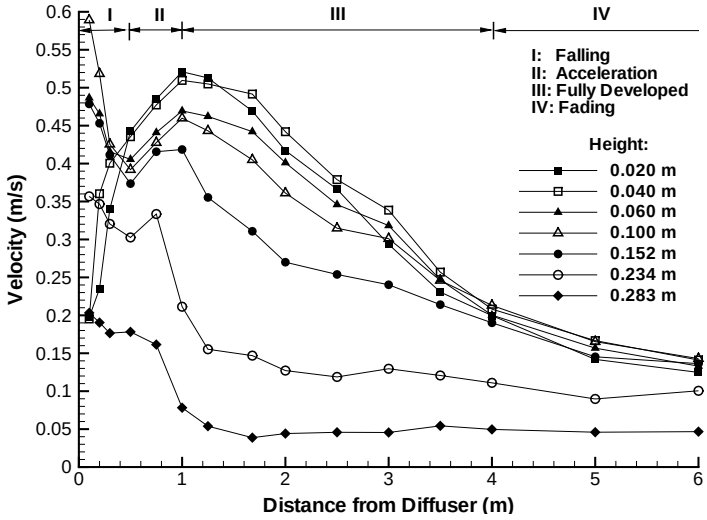

FIGURE 5.4: Horizontal velocity profiles at different heights inside the DV jet.

diffuser surface and ends 0.5 m downstream of it. Figures 5.4 and 5.6(a) demonstrate the DV jet development in this zone. The air velocity profile very close to the floor (for heights of 0.02 m and 0.04m) quickly ascends as the distance from the diffuser surface increases. However, within the same region, the magnitude of the velocity drops significantly as the measurement location elevates further.

5.2.2 Acceleration Zone

The reduction in the thickness of the jet envelope under the influence of buoyancy results in an initial acceleration of the flow in this zone. As shown in figures 5.4 and 5.6(b), in this region, the air velocity begins to increase about 0.5 m downstream of the diffuser surface and reaches its maximum at about 1 m.

5.2.3 Fully Developed Zone

Since the cross-sectional area of the jet increases with the distance from the corner, a reduction in the air velocity is expected in order to satisfy mass conservation. Figure 5.6(c) shows the vertical velocity profile in this region. As is evident, the jet profile keeps its shape between 1 m and 4 m downstream of the diffuser while

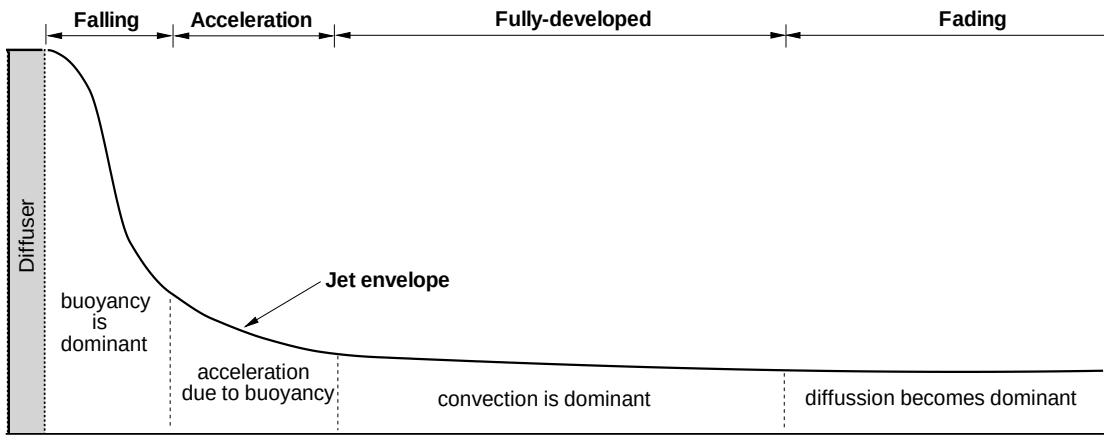

FIGURE 5.5: Development of a DV jet stream.

its magnitude decreases. The maximum velocity is located at about 0.04 m above the floor and is insensitive to the distance from the diffuser. These observations are consistent with the findings of Nielsen *et al.* [4], Brohus *et al.* [54] and Magnier *et al.* [10].

5.2.4 Fading Zone

In the far downstream region of the diffuser, heat transfer from the floor and the warmer air from above continue to reinforce the mixing and induction of the flow. As shown in figure 5.6(d), the mixing effect and vast lateral spread of the jet significantly decays the jet velocities and the mechanism of heat and momentum transfer is hence dominated by diffusion.

5.3 Comparison with Empirical Velocity Distribution Models

Figure 5.7 compares the modeled and measured values of the maximum jet velocity in the downstream region of the DV jet. The solid line shows the velocity prediction based on the model of Nielsen [3]. As seen from the figure, the horizontal maximum

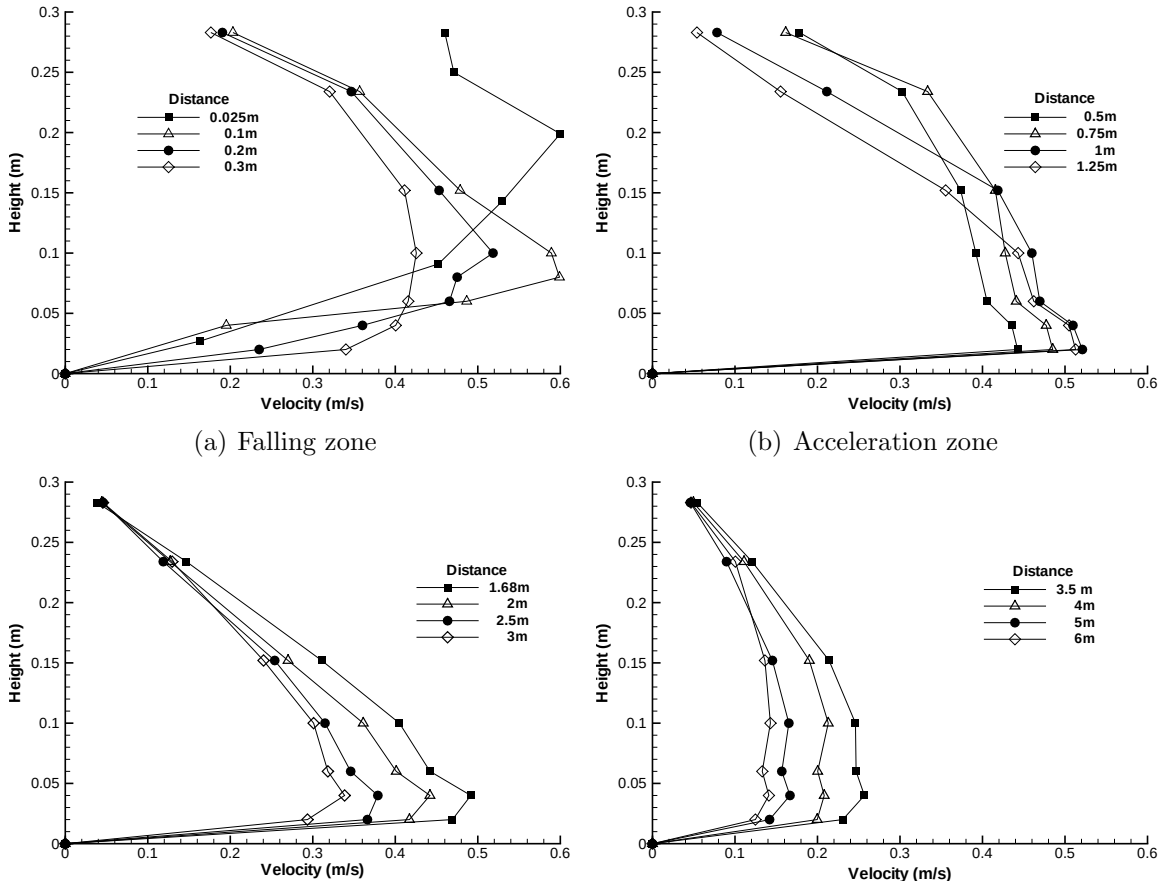

(a) Falling zone

(b) Acceleration zone

(c) Fully-developed zone

(d) Fading zone

FIGURE 5.6: Vertical profiles of the velocity inside the DV jet at different downstream distances from the diffuser.

velocity profile of the jet at height 0.04 m above the floor predicted using the empirical model is in good agreement with the experimental data.

Figures 5.8(a)-(c) compare the non-dimensionalized measured vertical velocity profiles in different zones of the DV jet with the predicted values based on the model of Verhoff [38] for an isothermal wall jet. In the acceleration zone, the non-dimensionalized measured values generate self-similar profiles which are slightly different from the isothermal profile. In this zone, owing to the buoyant forces, the airflow accelerates and changes its direction tangent to the floor. This physical mechanism is different from that of an isothermal wall jet. As is evident in figure 5.8(b), the non-dimensionalized velocity values in the fully-developed zone are

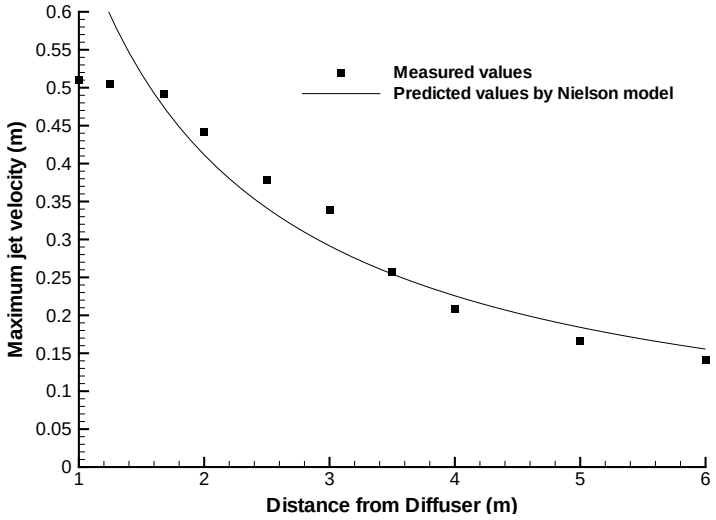

FIGURE 5.7: Comparison of the measured and predicted values of the jet maximum velocity.

in good agreement with the isothermal jet profile. Because of the relatively high velocity of the jet, the convection term dominates the buoyancy term, and therefore, the jet behaves like an isothermal wall jet in the fully-developed zone. Figure 5.8(c) shows that in the fading zone of the DV jet stream, the non-dimensionalized values of velocity do not match well with the isothermal profile of the wall jet. Because of the heat transfer from the floor, the air temperature increases in the near-floor region. This reinforces the buoyant forces within the jet and increases the diffusion of the momentum and thermal energy. Consequently, the flow distribution of the DV jet deviates from that of an isothermal jet.

Based on the above analysis, it is understood that in comparison with an isothermal wall jet, the behavior of the DV wall jet is altered by buoyancy. Although similarity still holds approximately in the velocity profile of the DV jet, the flow mechanism becomes more complicated. The development of the flow and the dominant flow mechanism in different zones are demonstrated in figure 5.5. So far, we have only focused our attention on the velocity field of the DV jet. In the next subsection, we will study the temperature field of the DV jet. We will further confirm the advantage of introducing those four zones into the physical analysis of the DV jet stream under investigation.

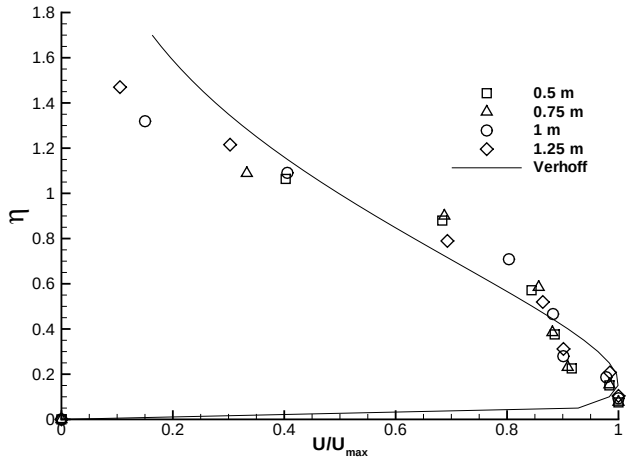

(a) Acceleration zone

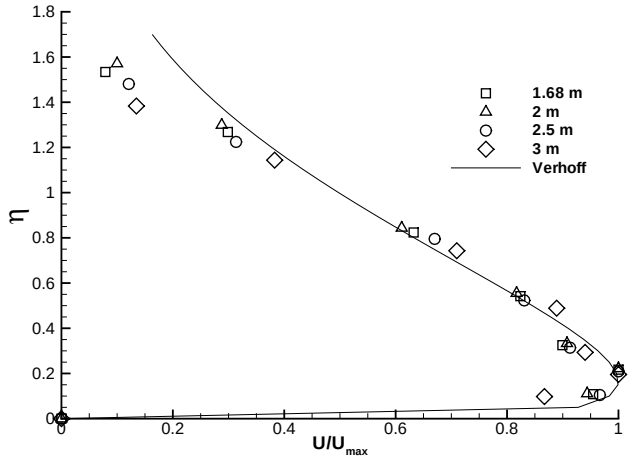

(b) Fully-developed zone

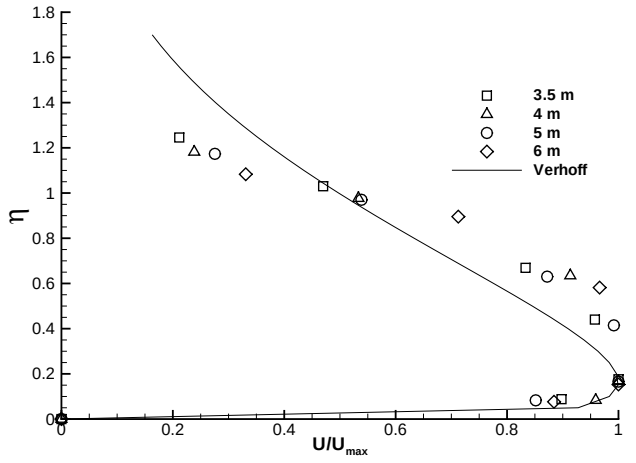

(c) Fading zone

FIGURE 5.8: Comparison of the non-dimensionalized measured vertical velocity profiles with the Verhoff model predictions.

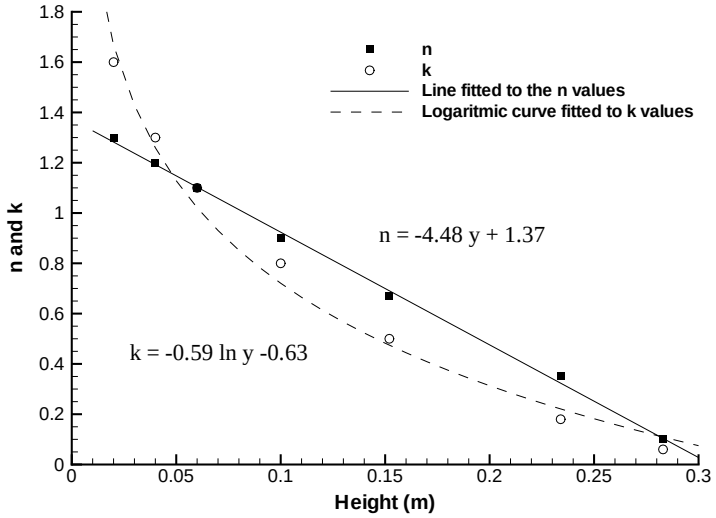

FIGURE 5.9: n and k values at different heights.

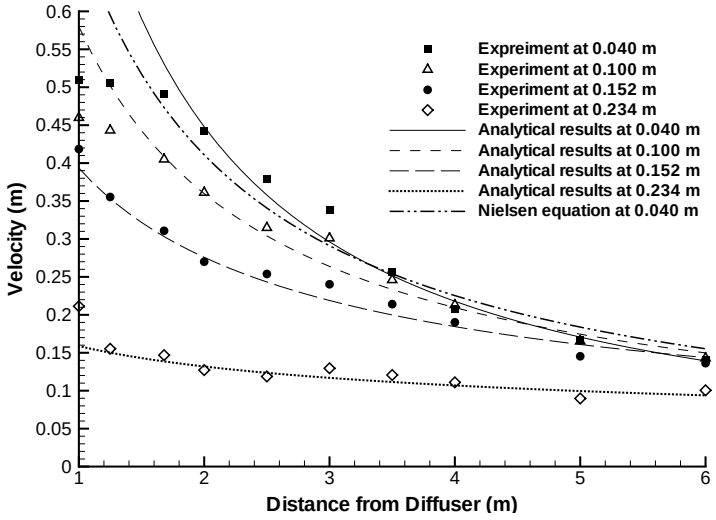

FIGURE 5.10: Comparison of experimental and analytical horizontal velocity profiles.

5.4 Velocity Distribution Model

In subsection 3.4 the DV jet velocity distribution models are introduced, including the conventional maximum velocity decay model of Neilsen [3], and a general DV velocity distribution model proposed by this research (which includes the Neilsen model as a special case). In the Neilsen model (equation 3.4), there are two constants, n and k. In the new model (equation 3.7), n and k are treated as variables in order to generalize the model for the entire DV jet, i.e. $n = \alpha_m y + \beta_m$ and $\kappa = \lambda_m ln y + \phi_m$.

In this subsection, this new model will be validated against the available experimental data.

Figure 5.9 displays the values of n and k with respect to the jet height y. As it can be seen from the figure, n and k can be represented as linear and logarithmic functions of y, respectively. For the proposed model, constants are determined as follows: $\lambda_m = -0.59$, $\phi_m = -0.63$, $\alpha_m = -4.48$ and $\beta_m = 1.37$ based on a regression analysis of the current experimental data.

Figure 5.10 compares the modeled and measured values of the horizontal velocity profiles at different heights in the downstream region of the DV jet. As it can be seen, the horizontal velocity profile of the jet at height 0.04 m above the floor predicted using the proposed model is in good agreement with the experimental data and the prediction of the Nielsen model [3]. Figure 5.10 also shows the horizontal velocity profiles at different heights calculated by the proposed model. As evident from the figure, the predictions from the model are in good agreement with the experimental data as a result of regression analysis.

5.5 Experimental Results on Temperature Distribution

As introduced in section 2, the temperature field was measured using both RTDs and infrared whole-field camera. In this subsection, experimental data acquired by these two different types of sensors will be analyzed subsequently.

5.5.1 Measurements Based on RTDs

Figure 5.11 displays the contour of air temperature inside and above the DV jet at different downstream locations of the diffuser. As shown in figure 5.11, in the region close to the diffuser, owing to the buoyancy, the cold air from the diffuser moves downward and warmer air moves upward, forming a vertical temperature gradient.

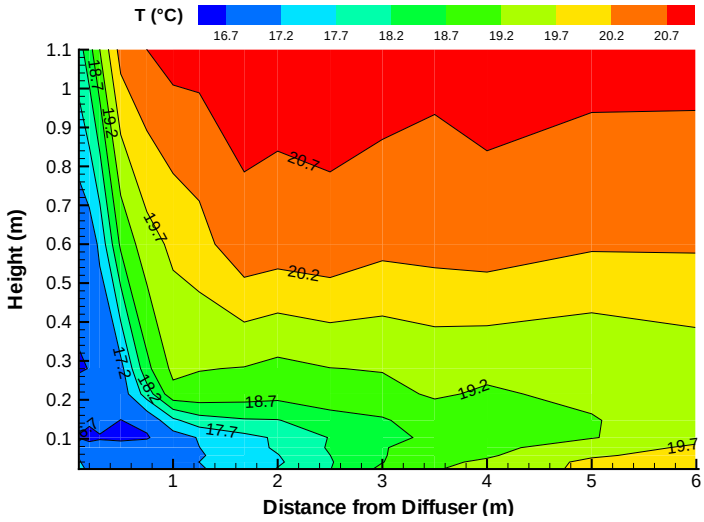

FIGURE 5.11: Contour of temperature in the measurement plane inside and above the DV jet.

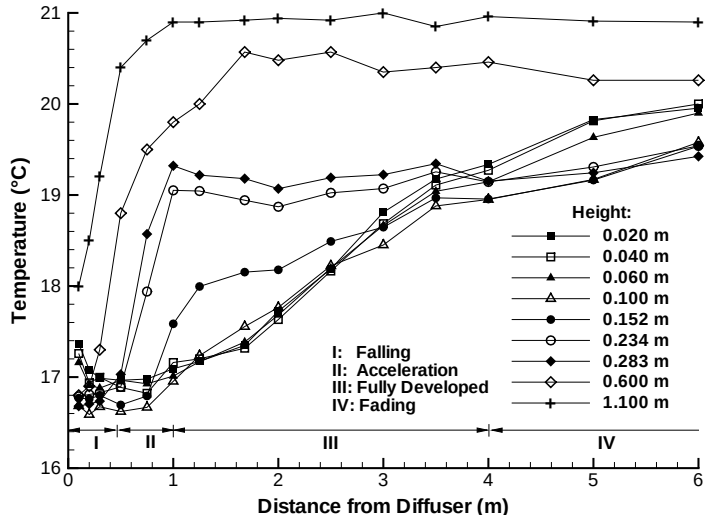

FIGURE 5.12: Horizontal temperature profiles at different heights inside and above the DV jet.

This works against mixing and induction of the flow, and leads to the formation of an interface (or, jet envelope) between the cold air of the DV jet and the warmer background air above it.

Figure 5.12 shows the horizontal temperature profiles at different heights. As it can be seen, the air temperature inside the jet increases as the distance from the diffuser increases. The values of the measured temperature quickly rise for higher elevations in a short distance from the diffuser (especially for curves corresponding to

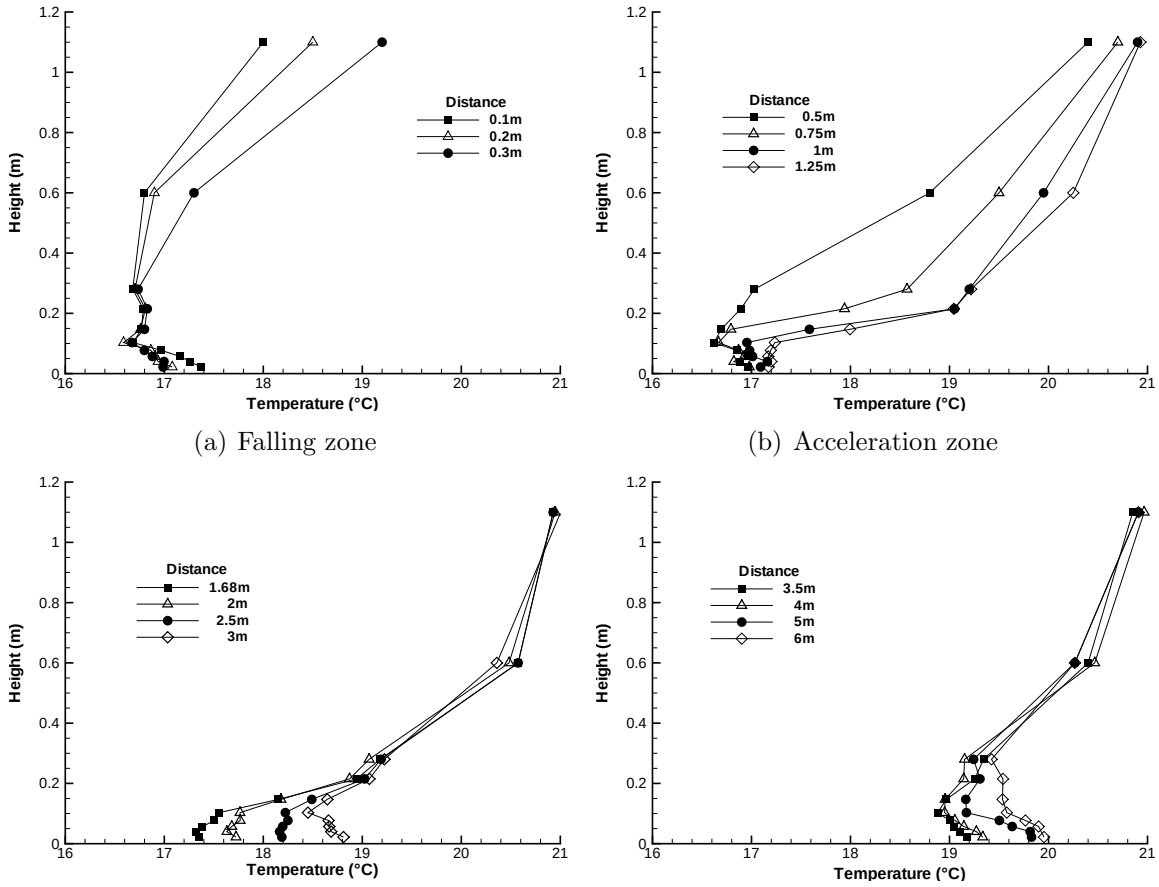

(a) Falling zone

(b) Acceleration zone

(c) Fully-developed zone

(d) Fading zone

FIGURE 5.13: Vertical profiles of the temperature inside and above the DV jet at different downstream distances from the diffuser.

elevations that are higher than 0.152 m). This confirms the observation of the small jet envelope height (prior to the falling zone) demonstrated previously by the smoke visualization test in figure 2.6 and the temperature contour in figure 5.11.

Figures 5.13(a-d) show the development of the temperature field inside and above the DV jet corresponding to the four velocity zones. As is evident in figures 5.13(a-d), in the near-floor region inside the jet, the air temperature is relatively high due to the heat transfer from the floor. However, above the jet, the air temperature is almost independent of the distance from the diffuser. These findings are consistent with the results of Li *et al.* [8] and Magnier *et al.* [10]

Figure 5.13(a) shows the vertical profiles of the air temperature in the falling zone

of the DV jet. Because of the massive downdraft of the cold air near the diffuser, the temperature profiles show a rather constant level in the near-floor region. However, at height 1.1 m (close to the diffuser top), the temperature increases significantly as the distance from the diffuser increases, indicating that a sharp horizontal temperature gradient exists close to the diffuser top to reflect the finite horizontal thickness of the cold downdraft.

In the acceleration zone, the thickness of the jet significantly reduces due to the horizontal spread of the jet flow on the floor. As seen in figure 5.13(b), there is a rapid rise in the temperature in the region above 0.1 m.

The vertical air temperature profiles in the fully-developed region are shown in figure 5.13(c). In this zone, because the convection term dominates the diffusion, the temperature gradient is large at the jet interface and small in the vicinity of the floor. As the distance from the diffuser increases, the near-floor temperature of the air increases monotonically. Above the jet, the air temperature is rather constant, independent of the distance from the diffuser.

Figure 5.13(d) shows the vertical profiles of temperature inside and above the fading velocity zone of the DV jet. In this region, the diffusion of the flow gradually becomes dominant (in comparison with convection). Because of the lower velocities of the jet, a relatively large gradient of temperature appears close to floor. Mixing increases between the jet and room air, and the jet interface becomes less apparent. Similar to the velocity field in this region, the air temperature inside the DV jet reaches the same order of magnitude of the temperature of the warmer air above the jet envelope.

5.5.2 Infrared Whole-field Thermography

In this experiment, an infrared whole-field camera and a measuring screen with a low emissivity were used to take the wall temperatures and air temperatures in a region near the diffuser. The setup of the camera and measuring screen is shown in figure 5.14. Two particular camera and screen positions are selected during the

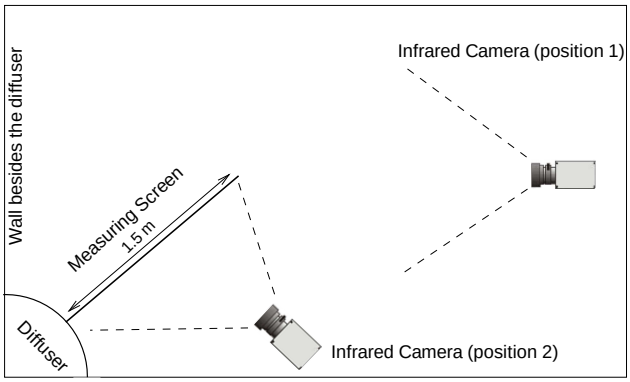

FIGURE 5.14: Positions of the infrared camera and measuring screen.

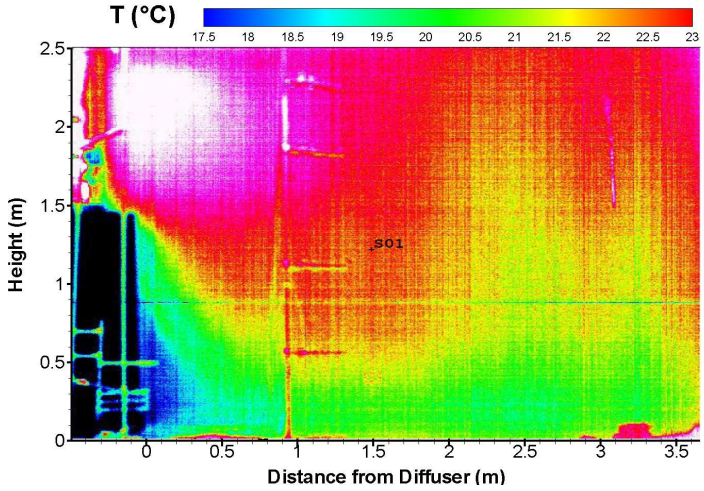

FIGURE 5.15: Infrared thermography measurement of the instantaneous wall temperature beside the diffuser (measured at camera position 1).

experiment: the camera is placed at position 1 to measure the temperature of the wall besides the diffuser, and at position 2 to capture the instantaneous temperature field in the near-zone of the diffuser.

Figure 5.15 shows the thermography of the wall besides the diffuser. It is clear from the figure that the wall temperature increases as the distance from the supply cold air increases. Characteristic of a room ventilated by a DV system, the airflow is stratified and a vertical temperature gradient exists in the room. This signature of the stratified temperature field is evident in figure 5.15. By comparing figures 5.16(a) and 5.16(b), the accuracy of the infrared thermography measurements in the near-zone of the diffuser can be evaluated. As shown in figures 5.16(a) and 5.16(b), the

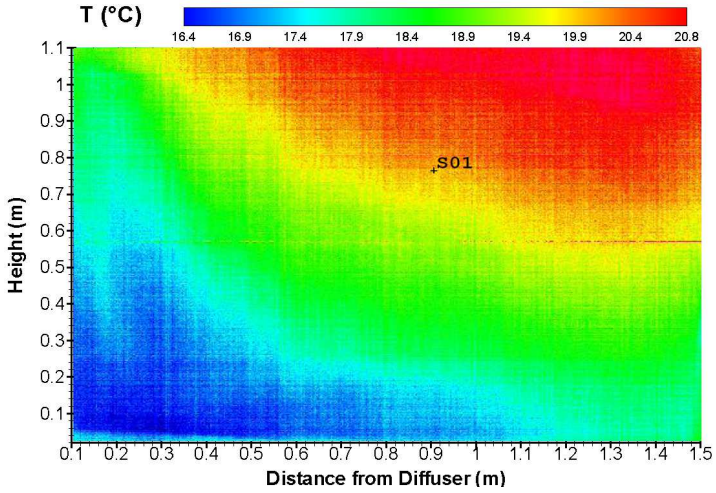

(a) Instantaneous temperature measured by infrared thermography (measured at camera position 2).

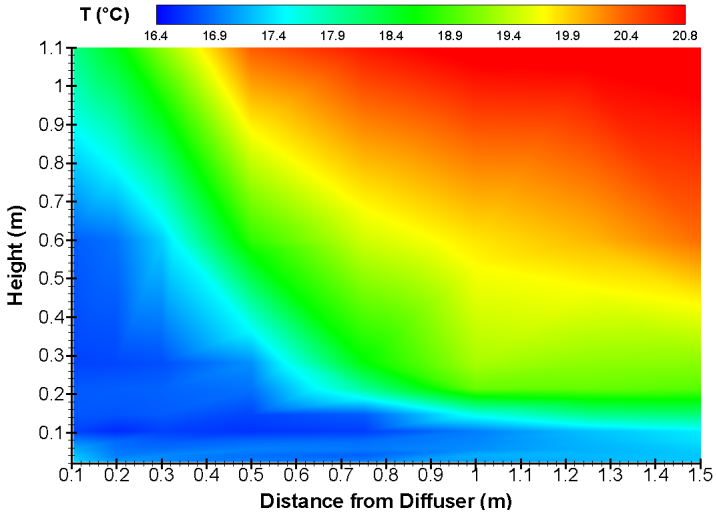

(b) Time averaged temperature measured using RTD.

FIGURE 5.16: Temperature isopleths in central measurement plane in the near-zone of the diffuser.

values measured by the infrared camera are in good qualitative agreement with the values measured using RTD probes. Furthermore, a careful comparison of figure 5.15 with figure 5.16(a) shows that the temperature distribution over the wall is similar to the air temperature distribution in the room; however, the wall temperatures are higher because the room air condition is on the cooling mode and heat is transferred into the room through the walls. In both figures 5.15 and 5.16(a), the cool air jet stream is well captured, and the interface (or, jet envelope) between the cool and warm airflows (shown using light blue color) is evident.

Cehlin *et al.* [55] performed a systematic study on infrared thermography measurement of the airflow in the near-zone of a displacement diffuser in order to analyze the influence of different parameters on the accuracy of the thermography technique. They identified several important parameters which include the radiation condition in the room, view angle of the camera, and emissivity and heat transfer coefficient of the screen. According to Cehlin *et al.* [55], the difference between the emissivity of the screen and that of the ambient air may result in a temperature difference between the screen and the air. In view of this, in this experiment, the selected screen has a low emissivity and the diffuser is far from the radiation panels, which led to a good accuracy in the infrared thermography measurement.

Although the infrared thermography can measure the air and wall temperatures with a high temporal resolution, it is more suitable for visualization and qualitative analysis of the temperature field. For advanced measurements of temperature, the accuracy of infrared thermography may not be satisfactory. In fact, it is challenging to use infrared thermography to measure a temperature field where large temperature gradients exist (e.g., the air temperature in the vicinity of the floor and at the interface of the DV jet). Furthermore, infrared thermography is sensitive to strong radiation fields. As it can be seen in figure 5.15, the wall temperature is affected in the upper left corner (indicated by the white and purple area in figure 5.15) close to the radiant heating panel.

5.6 Experimental Results on Turbulence Intensity

Figure 5.17 displays the horizontal profile of the turbulence intensity at height 0.04 m above the floor. As shown in the figure, the level of turbulence is minimum between 0.5 m and 2 m downstream of the diffuser. By comparing figures 5.4 and 5.17, the inverse relationship between the magnitudes of the velocity and turbulence intensity inside the DV jet reported by Magnier *et al.* [10] is confirmed.

The air velocity, temperature and turbulence intensity fields are tightly coupled

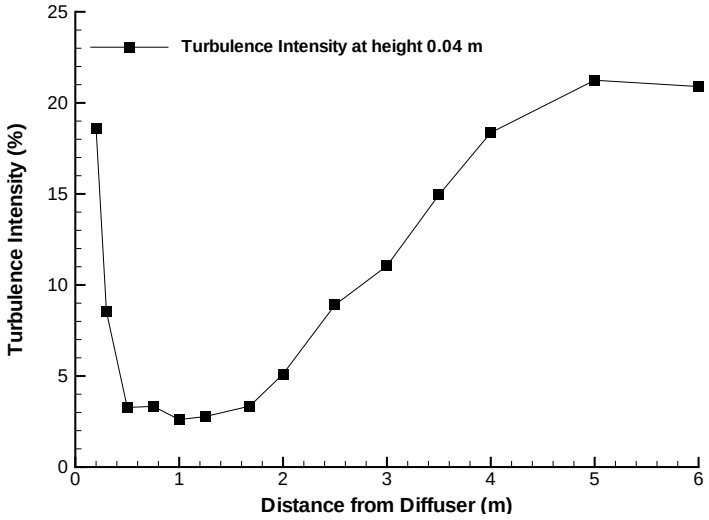

FIGURE 5.17: Turbulence intensity at height 0.04 m.

in a highly nonlinear manner (through the momentum and thermal energy transport equations). In other words, the magnitude of the velocity affects the level of turbulence intensity; the temperature gradients influence buoyancy, which further changes both the velocity field and turbulence intensity; and in return, the level of turbulence intensity determines the diffusion of thermal energy.

5.7 Experimental Results on Thermal Discomfort

Draft and vertical air temperature difference (VATD) are two major sources of thermal discomfort in rooms with DV systems. In this subsection, both factors are investigated based on the experimental measurements.

5.7.1 Draft Sensation

Draft is unwanted local cooling of body caused by cold air movement. Complaints of drafts are often associated with rooms equipped with DV systems, because the air is discharged directly into the occupied zone, producing relatively high speed and low temperature airflow at the lower-leg region. According to ASHRAE standard 55 [56], draft sensation depends on the air velocity, temperature and turbulence

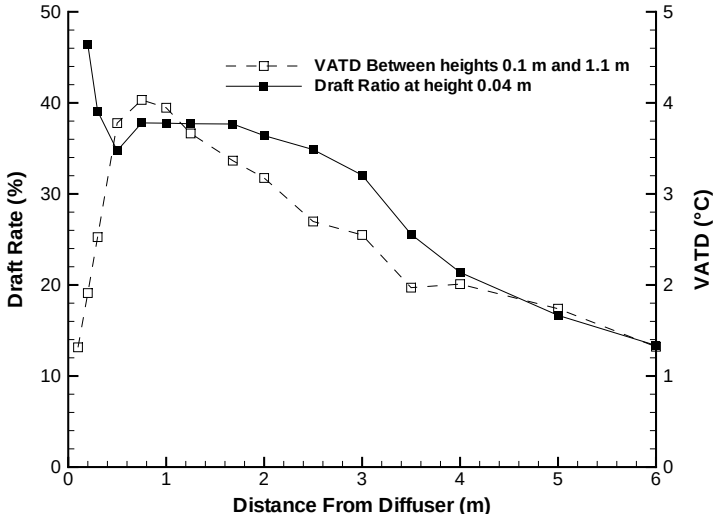

FIGURE 5.18: Draft rate and VATD.

intensity. Draft discomfort increases when the air temperature decreases and the mean air velocity and turbulence intensity increase. The predicted percentage of people dissatisfied due to the draft rate (DR) is given by:

$$DR = (34 - T) \times (v - 0.05)^{0.62}(0.37 \times v \times Tu + 3.14) \quad , \tag{5.1}$$

where T (°C) is the air temperature, v (m/s) is the mean velocity and Tu (%) is the turbulence intensity relative to the mean velocity of the flow. Figure 5.18 shows how the DR value changes with respect to the distance downstream of the diffuser at a particular height of 0.04 m. As expected, draft discomfort significantly decreases 4 m away from the diffuser in the fading zone of the DV jet.

5.7.2 Vertical Air Temperature Difference (VATD)

The difference in the surrounding air temperature over an occupant's body may also cause thermal discomfort. In contrast with traditional mixing ventilation systems, the air mixing and induction in rooms with DV systems is much smaller. In fact, the airflow is typically stratified in a room with a DV system, which can result in a relatively large temperature difference between the foot and head levels. According to ASHRAE standard 55 [56], in order to avoid thermal discomfort, the maximum

vertical air temperature difference between ankle and head levels for a seated person should be smaller than 3 °C. Figure 5.18 shows the VATD value between heights 0.1 m and 1 m (corresponding to the ankle and head levels for an average seated person, respectively) at different distances from the diffuser. The horizontal profiles of the air temperature have been shown previously in figure 5.12. In the downstream region of the diffuser, the VATD value decreases as the distance from the diffuser increases because the air temperature increases streamwise at height 0.1 m and but remains approximately constant streamwise at height 1.1 m. As shown in figure 5.18, the VATD value is below the threshold of thermal discomfort at downstream locations more than 3 m away from the diffuser.

5.8 Numerical Results

5.8.1 Performance of Supply Diffuser Models

The effect of the supply diffuser modeling on the numerical prediction of velocity and temperature fields is shown in figures 5.19 and 5.20. The numerical results presented in figures 5.19 and 5.20 are based on SST k-ω turbulence model which performed the best in comparison with other turbulence models. A performance evaluation of various turbulence models in terms of their prediction of velocity, temperature and turbulence intensity fields will be presented in the next subsection.

The predicted velocity profiles in figure 5.19 are based on three different inlet boundary condition treatment methods. As is evident from the figure, the method used to describe the diffuser has a major effect on the numerical prediction of the velocity field in near-zone of the diffuser. The proposed box-momentum method shows the best agreement with the experiment especially in the region immediately downstream of the diffuser (1.25 m from the diffuser). At distance 2 m from the diffuser, the momentum method shows a better accuracy in comparison with the box method. Far downstream of the diffuser, all modeling methods exhibit a similar accuracy, as all numerical predictions are in good agreement with the experimental

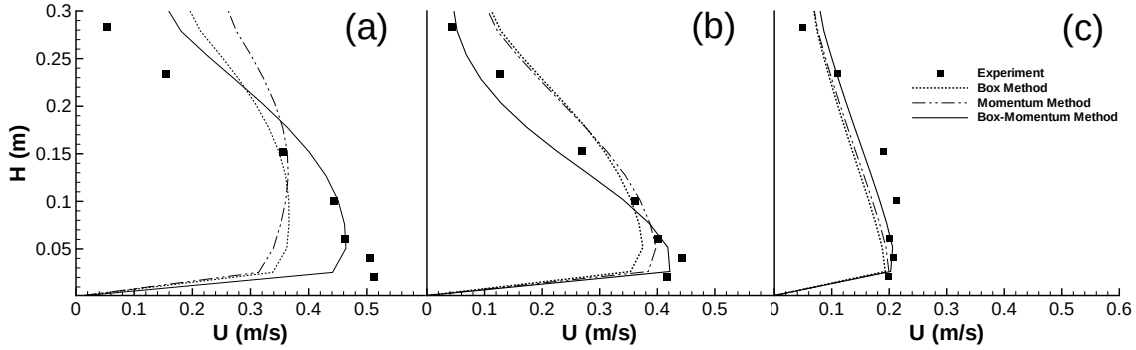

FIGURE 5.19: Comparison of predicted vertical velocity profiles using three diffuser models with the experimental data at different distances from the diffuser. (a): 1.25 m, (b): 2 m, (c): 4 m.

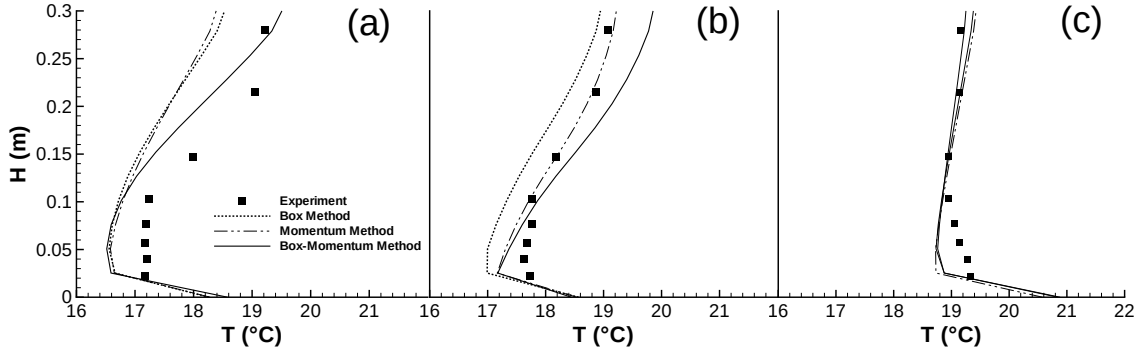

FIGURE 5.20: Comparison of predicted vertical temperature profiles using three diffuser models with the experimental data at different distances from the diffuser. (a): 1.25 m, (b): 2 m, (c): 4 m.

data. This clearly indicates that the effect of a diffuser supply model becomes less sensitive as the distance from the diffuser increases.

Similar to its predictive performance in calculating the velocity field, as is evident in figure 5.20, the proposed box-momentum method also shows the best performance in prediction of the temperature field, especially for the region near the diffuser. As shown in figures 5.19 and 5.20, the performance of the box method is similar to that of the momentum method, although the box method requires experimental measurements in establishing the supply boundary conditions.

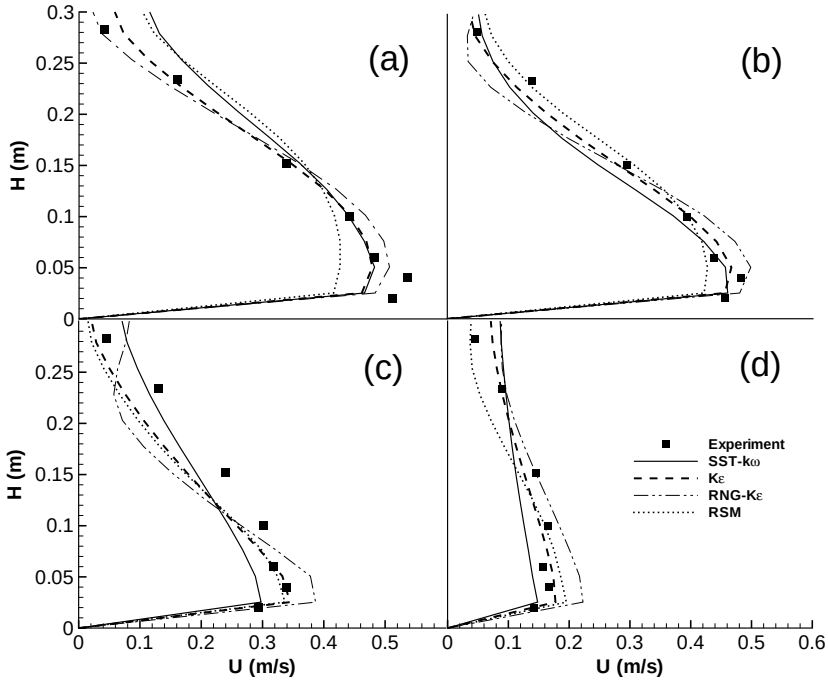

FIGURE 5.21: Comparison of predicted vertical velocity profiles using four turbulence models with the experimental data at different distances from the diffuser. (a): 1.68 m, (b): 2 m, (c): 3 m, (d): 5 m.

5.8.2 Performance of Turbulence Models

The performance of the turbulence models in terms of their prediction of the velocity and temperature fields at different downstream distances from the diffuser are shown in figures 5.21 and 5.22. The numerical results presented in these figures are based on the proposed box-momentum diffuser modeling method, which has been demonstrated to perform the best in comparison with other diffuser modeling methods.

As it can be seen in figure 5.21, all the turbulence models can predict the mean velocity profile with an acceptable accuracy. However, the predictive accuracy of the standard k-ϵ and SST k-ω models are the most satisfactory; as the numerical results predicted using these models are in the best conformance with the experimental data. Figure 5.21 shows that the RSM model underestimates the velocity peak values close to the diffuser (at the distances 1.68 m and 2 m away from the diffuser) and RNG k-ϵ overestimates the peak values at far downstream distances from the diffuser (3 m

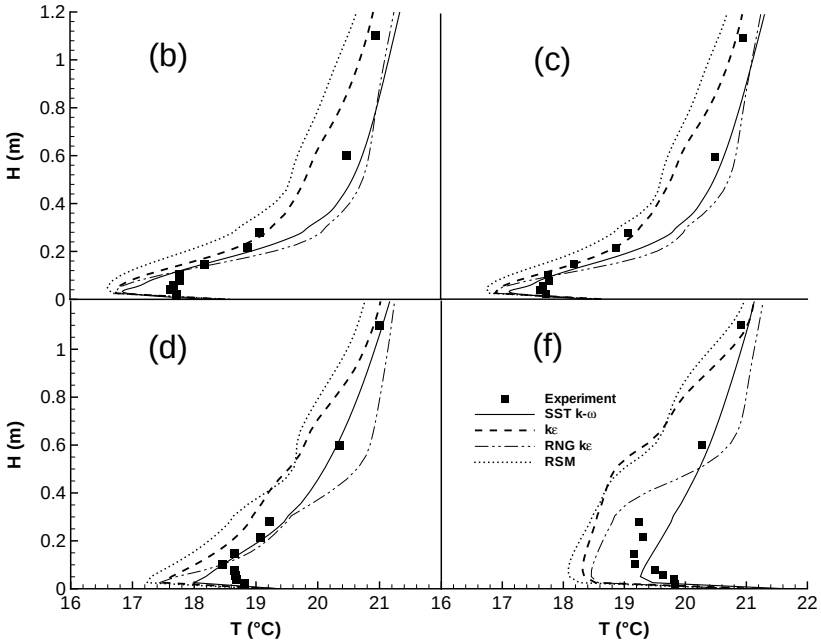

FIGURE 5.22: Comparison of predicted vertical temperature profiles using four turbulence models with the experimental data at different distances from the diffuser. (a): 1.68 m, (b): 2 m, (c): 3 m, (d): 5 m.

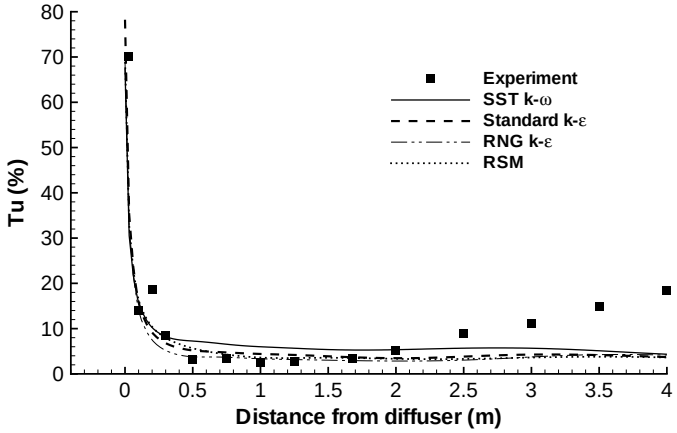

FIGURE 5.23: Prediction of horizontal profile of turbulence intensity using different turbulence models at height 0.04 m.

and 5 m away from the diffuser).

As demonstrated in figure 5.22, among the turbulence models used in this study, the predictive accuracy of the SST k-ω model is the most satisfactory in term of the calculation of the temperature, especially at the farthest downstream distance (5 m away from the diffuser). In comparison with the predictions of the standard

k-ϵ, RNG k-ϵ and SST k-ω models (which are conventional two-equation models), the result predicted by the RSM is the least satisfactory although the model formula for the RSM is much more complicated than those for the other models.

Figure 5.23 compares the predicted horizontal profiles of turbulence intensity by four turbulence models with the experimental values at height 0.04 m above the floor. As shown in figure 5.23, all the turbulence models could accurately predict the turbulence intensity in the near-zone of the diffuser. Far downstream of the diffuser, the turbulence models underestimate the turbulence intensity by 15%. Most turbulence models (including these four popular turbulence models tested) are usually well-validated in the context of shear flows (such as open channel flows in wind tunnels and water channels). The fact that the flow is weakly or even non turbulent in an indoor environment imposes great challenge to the test, design and modification of the turbulence models.

5.8.3 Numerical Results Based on the Box-momentum Supply Model Diffuser and SST k-ω Model

Figures 5.24 and 5.25 compare predicted vertical profiles of the velocity and temperature with experimental data at six different locations downstream of the diffuser. The numerical results are based on the box-momentum supply diffuser model and SST k-ω turbulence model, both of which have been proven to be the best among all the supply diffuser models and turbulence models tested.

As is evident in figure 5.24, the velocity profiles predicted by numerical simulations are in excellent agreement with the experimental data. Both the numerical and experimental results have successfully captured the strong shear layer ("nose" of the velocity profile) 0.3 m above the floor.

As shown in figure 5.25, the numerical results are in good conformance with the experiment data. Above the ankle level (about 0.1 m above the floor), most of the small discrepancies between numerical and experimental results fall under the

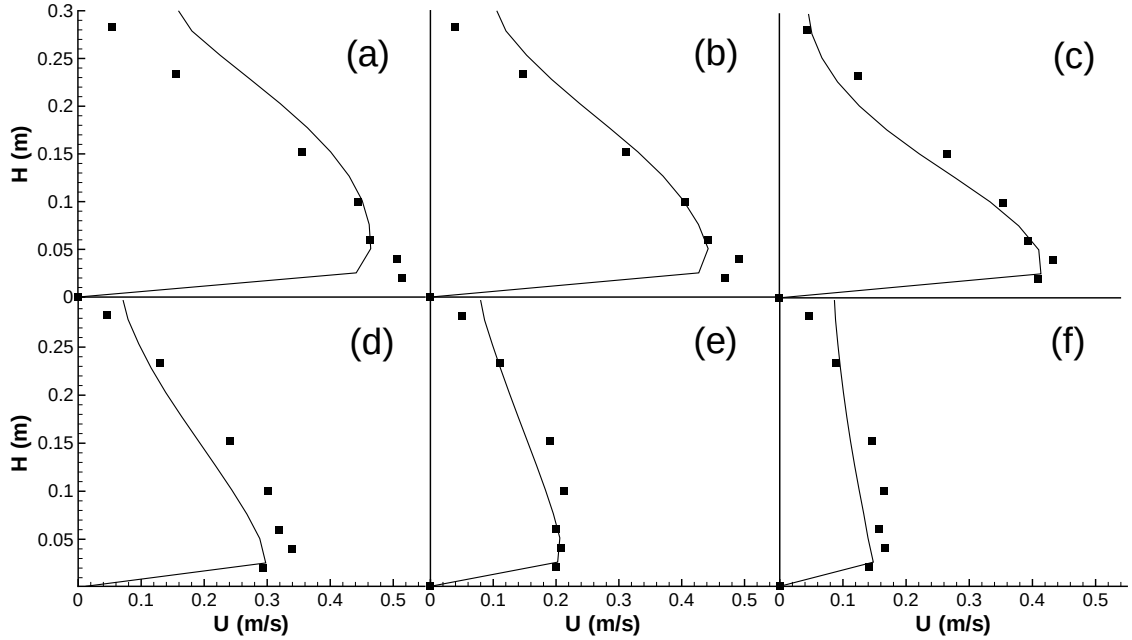

FIGURE 5.24: Vertical profiles of the velocity at different distances from the diffuser. (a): 1.25 m, (b): 1.68 m, (c): 2 m, (d): 3 m, (e): 4 m, (f): 5 m.

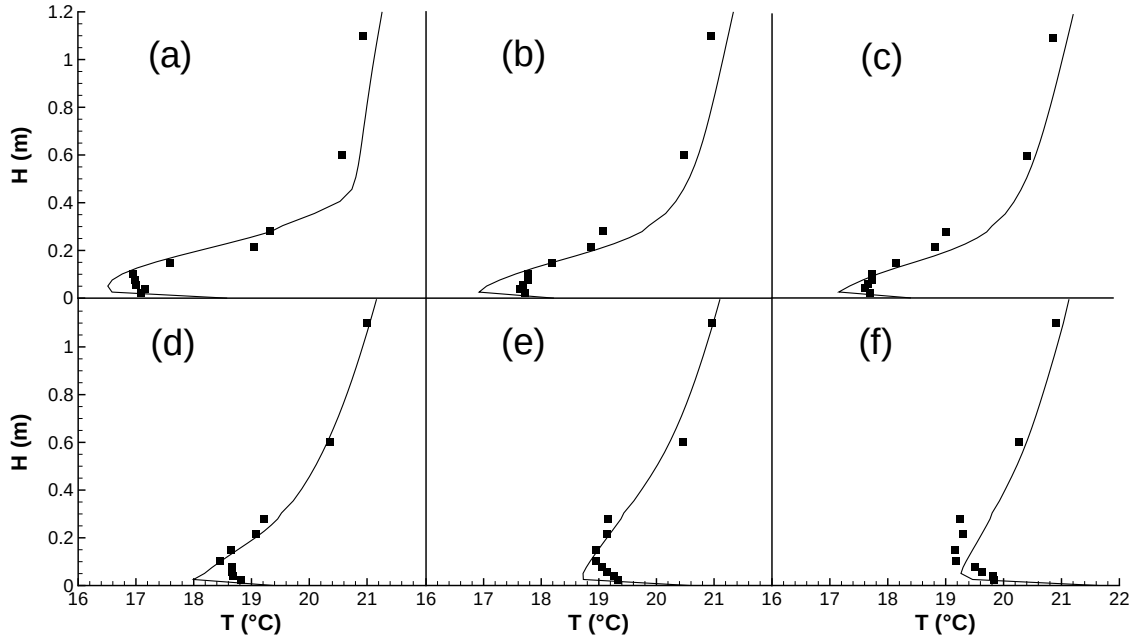

FIGURE 5.25: Vertical profiles of temperature at different distances from the diffuser. (a): 1.25 m, (b): 1.68 m, (c): 2 m, (d): 3 m, (e): 4 m, (f): 5 m.

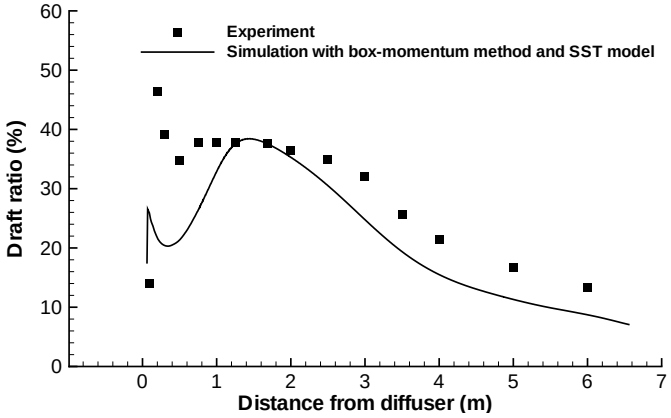

FIGURE 5.26: Draft ratio at the height of 0.04 m versus distance from the diffuser in the measurement plane.

measurement uncertainty threshold of the RTD sensors (which is 0.1 °C).

Figure 5.26 shows the calculated draft ratio based on numerical and experimental results at a particular height of 0.04 m along the jet. Far from the diffuser (L > 1.25 m), the values predicted by the numerical simulation are close to the experimental values. However in the region near to the diffuser (L < 1.0 m, non-occupied zone) the numerical simulation under-predicts the DR value.

Chapter 6

Conclusions and Future Work

The comprehensive data set obtained from this experiment allows for a refined physical analysis of the thermal jet flow generated by a large quarter-round corner-mounted displacement diffuser. It is observed that a floor-level DV jet stream can be divided into four zones, including the falling zone in which buoyant forces are dominant and push the cold dense airflow downwards, acceleration zone in which the reduction in the jet thickness under the influence of buoyancy results in an increase in the jet velocity, fully-developed zone in which the jet velocity profile keeps its shape, and fading zone where the jet velocity reduces significantly. The inlet boundary condition of the diffuser has been thoroughly measured and analyzed, and acquired data set is useful for further conducting and validating numerical simulations.

The measured maximum jet velocity values are in good agreement with the prediction of the empirical model of Nielsen [3]. In the fully-developed zone, inertial forces dominate buoyant forces and the jet behaves like an isothermal wall jet. For this reason, the measured velocity values match well with the empirical wall jet velocity profiles predicted by the classical Verhoff equation [38]. In other zones, buoyancy acts on the DV jet stream and forces its velocity distribution to deviate from that of an isothermal wall jet. This difference in the velocity distributions is small in the acceleration zone, but becomes more apparent in the fading zone.

In order to conquer the limitation of the existing models which focus only on the maximum velocity of the DV jet, an improved empirical model is proposed. This new

model is capable of predicting the jet velocity profile as a function of the jet height in the downstream region of the jet. Although the prediction of this proposed model is in good agreement with the experimental data, it is important to further examine its predictive performance based on other DV jet systems in future studies.

The temperature fields corresponding to different velocity zones have been thoroughly analyzed. In the region close to the diffuser, the airflow is stably stratified due to the existence of buoyant forces and the initial momentum of the cold air issued from the floor-mounted diffuser. As a result, an interface between the cold denser air of the DV jet and the warmer lighter air of the room is formed. Owing to the low entrainment rate of the warmer air, the temperature of the cool jet flow stays constant in the region near the diffuser. As the air flows on the floor, the thickness of the jet reduces significantly and sharp gradients of temperature occur at the jet interface. In the fully-developed region of the jet, the temperature of the jet increases gradually due to the heating effect of the floor. However, in the fading zone, thermal diffusion gradually becomes dominant as the jet interface gradually disappears.

The temperature values measured by infrared camera are in good agreement with the values measured using RTD probes. Although infrared thermography offers many advantages, its measurement accuracy is influenced by several factors, such as the screen emissivity rate and the distance between the measurement plane and heating radiation sources. In order to acquire high-quality measurement data, a low emissivity screen was used and placed far from the radiation sources in the experiment.

The detailed measurement data on air velocity, temperature and turbulence intensity allow for a thermal comfort analysis of the DV system. In general, draft and VATD discomfort reduces as the distance from the diffuser increases. Given the specific test condition, it is recommended that a person be seated at least 3 meters away from the diffuser in order to avoid any thermal discomfort.

The supply differ model has a major effect on the numerical prediction of the velocity and temperature fields in the region near the diffuser. In the downstream region of the diffuser, the momentum method have a better accuracy compare to the

box method. However, among all the supply diffuser models tested, the proposed box-momentum method shows the best agreement with the experiment especially in the region immediately downstream of the diffuser. Far downstream of the diffuser, all the diffuser modeling methods exhibit similar performances, as all numerical predictions are in good agreement with the experimental data.

Numerical results show that all the tested turbulent models predict the mean velocity profile with an acceptable accuracy. However, the predictive accuracy of the standard k-ϵ and SST k-ω models are the most satisfactory. Among the turbulence models used in this study, the SST k-ω model is the most satisfactory in terms of the prediction of the temperature, especially in the region far downstream of the diffuser. All the turbulence models could accurately predict the turbulence intensity in the near-zone. However, far downstream of the diffuser, the turbulence models underestimate the turbulence intensity. Most turbulence models (including these four popular turbulence models tested) are usually well-validated in the context of shear flows (such as open channel flows in wind tunnels and water channels). The fact that the flow is weakly or even non turbulent in an indoor environment imposes great challenge to the test, design and modification of the turbulence models.

The draft ratio values predicted by CFD simulation are very close to the experimental values in the downstream region of the diffuser. However, in the non-occupied zone near the diffuser, the numerical simulation under-predicts the DR value.

The comprehensive experimental data set compiled in this research could be very useful for improved design of DV systems and for better understanding of the flow physic of a DV jet. In the future, in order to further generalize the empirical models for DV jets velocity and temperature distribution, data sets for DV jets with different Archimedes numbers need to be provided. Finally, further validations of the proposed box-momentum diffuser modeling approach for DV systems in contexts of other supply diffusers are necessary to confirm its advantageous performances.

References

[1] H. Skistad, *Displacement Ventilation*. Taunton, Somerset, England: Research Studies Press Ltd., 1994.

[2] Q. Chen and L. Glicksman, *System performance evaluation design guidelines for displacement ventilation*. Georgia, Atlanta: ASHRAE, 2003.

[3] P. V. Nielsen, "Velocity distribution in a room ventilated by displacement ventilation and wall-mounted air terminal devices," *Energy and Buildings*, vol. 31(3), pp. 179–187, 2000.

[4] P. V. Nielsen, L. Hoff, and L. G. Pedersen, "Displacement ventilation by different types of diffusers," in *Proceedings of 9th AIVC Conference, Effective Ventilation*, (Gent, Belgium), 1988.

[5] T. Zhang, K. Lee, and Q. Chen, "A simplified approach to describe complex diffusers in displacement ventilation for CFD simulations," *Indoor Air*, vol. 19, pp. 255–267, 2009.

[6] J. Lau and Q. Chen, "Floor-supply displacement ventilation for workshops," *Building and Environment*, vol. 42, pp. 1718–1730, 2007.

[7] G. Einberg, K. Hagstrom, P. Mustakallio, H. Koskela, and S. Holmberg, "CFD modelling of an industrial air diffuser–predicting velocity and temperature in the near zone," *Building and Environment*, vol. 40, pp. 601–615, 2005.

[8] Y. Li, M. Sandberg, and L. Fuchs, "Vertical temperature profiles in rooms ventilated by displacement: Full-scale measurement and nodal modelling," *Indoor Air*, vol. 2, pp. 225–243, 1992.

[9] M. Cehlin and B. Moshfegh, "Numerical modeling of a complex diffuser in a room with displacement ventilation," *Building and Environment*, vol. 45, pp. 2240–2252, 2010.

[10] L. Magnier, R. Zmeureanu, and D. Derome, "Experimental assessment of the velocity and temperature distribution in an indoor displacement ventilation jet," *Building and Environment*, vol. 47, pp. 150–160, 2012.

[11] N. Rajaratnam, *Turbulent Jets*. Elsevier, 1976.

[12] Nordic Innovation Center, *NORDTEST method for air terminal devices: Aerodynamic testing and rating at low velocity, NT VVS 083*. 2nd ed., 2012.

[13] J. Srebric and Q. Chen, "Simplified numerical models for complex air supply diffusers," *HVAC&R Research*, vol. 8(3), pp. 277–294, 2002.

[14] M. Skovgard and P. V. Nielsen, "Modelling complex inlet geometries in CFD – applied to air flow in ventilated rooms," in *Proceedings of 12th AIVC Conference, Air Movement and Ventilation Control within Buildings*, vol. 3, (Ottawa, Canada), pp. 183–200, 1991.

[15] J. R. Fontaine, R. Rapp, H. Koskela, and R. Niemela, "Evaluation of air diffuser flow modelling methods experiments and computational fluid dynamics simulations," *Building and Environment*, vol. 40, pp. 377–389, 2005.

[16] Y. Sun and T. F. Smith, "Air flow characteristics of a room with square cone diffusers," *Building and Environment*, vol. 40, pp. 589–600, 2005.

[17] J. Heikkinen, "Modeling of a supply air terminal for room air flow simulation," in *Proceedings of 12th AIVC Conference, Air Movement and Ventilation Control within Buildings*, vol. 3, (Ottawa, Canada), pp. 213–230, 1991.

[18] P. Emvin and L. Davidson, "A numerical comparison of three inlet approximations of the diffuser in case E1 Annex 20," in *Proceedings of 5th Conference on Air Distributions in Rooms, ROOMVENT 96*, vol. 1, (Yokohama, Japan), pp. 219–226, 1996.

[19] Q. Chen and J. Moser, "Simulation of a multiple-nozzle diffuser," in *Proceedings of 12th AIVC Conference, Air Movement and Ventilation Control within Buildings*, vol. 2, (Ottawa, Canada), pp. 1–14, 1991.

[20] P. V. Nielsen, *The box method – A practical procedure for introduction of an air terminal device in CFD calculation.* Denmark: Instituttet Bygningsteknik, Aalborg University, 1997.

[21] H. T. Xu and J. L. Niu, "A new method of CFD simulation of airflow characteristics of swirling floor diffusers," in *Proceeding of 8th International IBPSA Conference*, (Eindhoven, Netherlands), pp. 1429–1434, 2003.

[22] J. Srebric and Q. Chen, "A method of test to obtain diffuser data for CFD modeling of room airflow," *ASHRAE Transaction*, vol. 107, pp. 108–116, 2000.

[23] S. Luo and B. Roux, "Modeling of the HESCO nozzle diffuser used in IEA Annex-20 experiment test room," *Building and Environment*, vol. 39(4), pp. 367–384, 2004.

[24] S. Luo, J. Heikkinen, and B. Roux, "Simulation of air flow in the IEA Annex 20 test room–Validation of a simplified model for the diffuser in isothermal test cases nozzle," *Building and Environment*, vol. 39(12), pp. 1403–1415, 2004.

[25] P. V. Nielsen, "The selection of turbulence models for prediction of room airflow," *ASHRAE Transactions*, vol. 104(1), pp. 1119–1127, 1998.

[26] Q. Chen, "Comparison of different k-ϵ models for indoor air flow computations," *Numerical Heat Transfer*, vol. 28, pp. 353–369, 1995.

[27] Q. Chen, "Prediction of room air motion by Reynolds-stress models," *Building and Environment*, vol. 31(3), pp. 233–244, 1996.

[28] F. Kuznik, G. Rusaouen, and J. Brau, "Experimental and numerical study of a full scale ventilated enclosure: Comparison of four two equations closure turbulence models," *Building and Environment*, vol. 42, pp. 1043–1053, 2007.

[29] Z. Zhai, Z. Zhang, W. Zhang, and Q. Chen, "Evaluation of various turbulence models in predicting airflow and turbulence in enclosed environments by CFD: Part 1–Summary of prevalent turbulence models," *HVAC&R Research*, vol. 13(6), pp. 853–870, 2007.

[30] Z. Zhang, W. Zhang, Z. Zhai, and Q. Chen, "Evaluation of various turbulence models in predicting airflow and turbulence in enclosed environments by CFD: Part 2–Comparison with experimental data from literature," *HVAC&R Research*, vol. 13(6), pp. 871–886, 2007.

[31] B. E. Launder and D. B. Spalding, "The numerical computation of turbulent flows," *Computer Methods in Applied Mechanics and Engineering*, vol. 3, pp. 269–289, 1974.

[32] L. Davidson, "Ventilation by displacement in a three-dimensional room–A numerical study," *Building and Environment*, vol. 24(4), pp. 363–372, 1989.

[33] V. Yakhot and S. A. Orszag, "Renormalization group analysis of turbulence. I. Basic theory," *Journal of Scientific Computing*, vol. 1, pp. 3–51, 1986.

[34] X. Yuan, Q. Chen, L. R. Glicksman, Y. Hu, and X. Yang, "Measurements and computations of room air-flow with displacement ventilation," *ASHRAE Transactions*, vol. 105(1), pp. 340–352, 1999.

[35] X. Yuan, Q. Chen, and L. R. Glicksman, "Models for prediction of temperature difference and ventilation effectiveness with displacement ventilation," *ASHRAE Transactions*, vol. 105(1), pp. 353–367, 1999.

[36] L. Zhang, T. T. Chow, Q. Wang, K. F. Fong, and L. S. Chan, "Validation of CFD model for research into displacement ventilation," *Architectural Science Review*, vol. 48, pp. 305–316, 2005.

[37] A. Stamou and I. Katsiris, "Verification of a CFD model for indoor airflow and heat transfer," *Building and Environment*, vol. 41(9), pp. 1171–1181, 2006.

[38] A. Verhoff, *The two-dimensional turbulent wall jet with and without an external free stream, Report 626.* Princeton University, 1963.

[39] ASHRAE, *ANSI/ASHRAE Standard 113: Method of testing for room air diffusion.* Atlanta, Georgia, 2005.

[40] W. Finkelstein, A. K. Melikov, T. Sefker, and G. Langkilde, "Laser Doppler measurements of airflow characteristics in rooms with mechanical ventilation," in *Proceedings of the 7th International Conference on Indoor Air Quality and Climate*, vol. 3, (Nagoya, Japan), pp. 785–790, 1996.

[41] Y. Sun and Y. Zhang, "An overview of room air motion measurement: Technology and application," *HVAC&R Research*, vol. 13(6), pp. 929–950, 2007.

[42] P. J. Christman and J. Podzimek, "Hot-wire anemometer behaviour in low velocity air flow," *Journal of Physics E: Scientific Instruments*, vol. 14, pp. 46–51, 1981.

[43] A. K. Melikov, Z. Popiolek, M. C. G. Silva, I. Care, and T. Sefker, "Accuracy limitations for low-velocity measurements and draft assessment in rooms," *HVAC&R Research*, vol. 13(6), pp. 971–986, 2007.

[44] I. Fatemi, B.-C. Wang, S. N. Oskouie, M. Koupriyanov, and B. Tully, "Numerical modeling of a displacement diffuser using an improved momentum method," in *Proceedings of the Canadian Society for Mechanical Engineering International Congress*, (Winnipeg, Canada), 2012.

[45] E. Forthmann, "Turbulent jet expansion," *Ingenieur-Archive*, vol. 5(1), pp. 42–54, 1934. NACA Technical Memorandum 789.

[46] A. Sigalla, "Measurements of skin friction in a plane turbulent wall jet," *Journal of the Royal Aeronautical Society*, vol. 62, pp. 873–877, 1958.

[47] G. E. Myers, J. J. Schauer, and R. H. Eustis, "Plane turbulent wall jet flow development and friction factor," *Journal of Basic Engineering*, vol. 85, pp. 47–53, 1963.

[48] W. H. Schwarz and W. P. Cosart, "The two-dimensional turbulent wall-jet," *Journal of Fluid Mechanics*, vol. 10, pp. 481–495, 1961.

[49] J. H. Ferziger and M. Peric, *Computational methods for fluid dynamics*. Berlin: Springer, 2001.

[50] D. C. Wilcox, *Turbulence modeling for CFD*. La Canada, California: DCW Industries Inc., 2006.

[51] Fluent Inc., *Fluent Manual, Fluent 6.3*. 2006.

[52] B. E. Launder, G. J. Reece, and W. Rodi, "Progress in the development of a Reynolds-stress turbulence closure," *Journal of Fluid Mechanics*, vol. 68(3), pp. 537–566, 1975.

[53] C. G. Speziale, S. Sarkar, and T. B. Gatski, "Modelling the pressure-strain correlation of turbulence: An invariant dynamical systems approach," *Journal of Fluid Mechanics*, vol. 227, pp. 245–272, 1991.

[54] H. Brohus and P. V. Nielsen, "Personal exposure in displacement ventilated rooms," *Indoor Air*, vol. 6, pp. 157–167, 1996.

[55] M. Cehlin, B. Moshfegh, and M. Sandberg, "Measurement of air temperatures close to a low-velocity diffuser in displacement ventilation using an infrared camera," *Energy and Buildings*, vol. 34, pp. 687–698, 2002.

[56] ASHRAE, *ANSI/ASHRAE Standard 55: Thermal environmental conditions for human occupancy*. Atlanta, Georgia, 2004.